Carbon 153 (2019) 513–524

Contents lists available at ScienceDirect

Carbon

journal homepage: www.elsevier.com/locate/carbon

Anisotropic mechanical properties and strengthening mechanism in superaligned carbon nanotubes-reinforced aluminum

Jong Gil Park [a, b], Jeong-Gyun Kim [a, b], Kang Pyo So [c], Jun Yeon Hwang [d], Eun Sung Kim [e], Ju Li [c], Dongseok Suh [a, b], Young Hee Lee [a, b, f, *]

[a] Center for Integrated Nanostructure Physics (CINAP), Institute for Basic Science (IBS), Suwon, 16419, Republic of Korea
[b] Department of Energy Science, Sungkyunkwan University, Suwon, 16419, Republic of Korea
[c] Department of Nuclear Science and Engineering, Department of Materials Science and Engineering, Massachusetts Institute of Technology, Cambridge, MA, 02139, USA
[d] Institute of Advanced Composite Materials, Korea Institute of Science and Technology (KIST), Jeonbuk, 55324, Republic of Korea
[e] R&D Center, A-Tech System Co., 18 Annam-ro 369 beon-gil, Bupyeong-gu, Incheon, 21312, Republic of Korea
[f] Department of Physics, Sungkyunkwan University, Suwon, 16419, Republic of Korea

ARTICLE INFO

Article history:
Received 7 May 2019
Received in revised form
3 July 2019
Accepted 10 July 2019
Available online 10 July 2019

ABSTRACT

High-strength carbon nanotubes (CNTs) enhance the mechanical properties in metal matrix composites; however, their extremely high aspect ratio leads to the anisotropy of mechanical properties. This underlying issue has not yet been clarified owing to the complicated multiple strengthening mechanisms. Herein, we report the anisotropic mechanical properties of a CNT-reinforced aluminum composite and strengthening mechanisms. The uniaxial alignment of CNTs and control of alignment angles were achieved via a mechanical pulling method using a vertically grown CNT forest. As a result, the modulus and strengths decreased in proportion to the misorientation angle. Owing to the superaligned CNTs, the experimental tensile strength in the iso-strain state of the Al-0.15 vol% CNT composite (improved by 20.1%) was near the theoretical value (21.8%), and the strengthening efficiency of the composite was ~1000. On the other hand, there was a significant deviation between the experimental result and theoretical value in the iso-stress state of the composites. This unusual anisotropic tendency was demonstrated by the strengthening effect of the CNT bridges, which tied the aligned CNTs together, in line with the interconnecting model. The anisotropic mechanical properties corroborate well with our predicted model from calculation by the failure criterion theory with the interconnecting model.

1. Introduction

Metals processed by alloying techniques play a critical role as engineering materials in the modern industry and drive an annual market worth trillions of dollars. However, the use of metal alloys is limited in harsh environments owing to their strengthening limitation and instability of strengthening media (precipitation phases). In this regard, exploring stable inclusions of nanomaterials in the metallic matrix will be a sensible approach to overcome the design limitation of materials. Among the various nanoreinforcement materials employed in metal matrix composite (MMC) systems, one-dimensional (1D) carbon nanotubes (CNTs) are a good candidate owing to their ultra-high mechanical strength, high stability, and extremely high aspect ratio [1–4]. In the strengthening mechanism of a 1D materials-reinforced composite, the misorientation angle (θ) of the aligned materials relative to the loading direction during the tensile test is a major factor. When the reinforced material is aligned in parallel with the loading direction ($\theta = 0°$, iso-strain state), the improvement of the mechanical strength is maximized (Fig. S1, Supporting Information) [5,6]. Therefore, many researchers have been focusing on the alignment method and increasing mechanical properties of the iso-strain state of CNTs reinforced MMC [4,7–11]. However, the aligned CNTs-reinforced composite has an anisotropy of mechanical properties because the variation of misorientation angle leads to the change in failure mode and internal force dispersion between the matrix and reinforcement of CNT [5,12]. Besides, those phenomena occur simultaneously with various strengthening effects of CNTs such as

* Corresponding author. Center for Integrated Nanostructure Physics (CINAP), Institute for Basic Science (IBS), Suwon, 16419, Republic of Korea.
E-mail address: leeyoung@skku.edu (Y.H. Lee).

https://doi.org/10.1016/j.carbon.2019.07.035
0008-6223/

an Orowan looping system, a generation of dislocations by the thermal mismatch, and a grain refinement. Owing to such complexity of strengthening mechanisms, the underlying the mechanical anisotropy issue in the CNTs-reinforced composite has not yet been clarified [13] although such anisotropic information is critical for the material and structural design to commercialize into the real industry. Herein, we report the anisotropy of mechanical properties and strengthening mechanisms in the CNTs-reinforced aluminum composite with a specific design and fabrication method. In previous studies, although the added CNTs were aligned along the deforming direction of the matrix during the process such as rolling and extrusion [4,7–11], the micro-scale deformation is not sufficient to uniaxially align nanoscale CNTs [10,14]. To overcome this issue, we aligned CNTs along the pulling direction horizontally from a vertically grown CNT forest using a mechanical pulling method [15]. In addition, as strong bonding between the matrix and reinforcement is an essential condition to improve the mechanical strength of composite materials, the formation of an atomically fused (or chemically bonded) interface and the removal of diffusion barriers such as oxide layers on the metal surface are required to achieve high performance [16]. Therefore, the same metal atoms were deposited on the CNT surface via sputtering under high vacuum [17], which prevents the direct contact between the oxide layer and CNT surface. Also, to maximize the anisotropic behavior of mechanical properties, the strengthening mechanisms which are not related to the alignment direction of CNTs were artificially suppressed by adopting a laminated structure [18,19]. Our approach sheds light on the high strengthening efficiency and anisotropy of the mechanical properties via systematic analysis of their strengthening mechanisms in the CNT-reinforced aluminum composite.

2. Experimental section

2.1. Synthesis of Al-CNT composite

The fabrication method of the superaligned CNT-reinforced Al composite consists of five steps, as shown in Fig. 1a: (i) mechanically drawing one edge of the CNT forest as a sheet form; (ii) transfer of the suspended CNT sheet onto the Al foil; (iii) the deposition of Al atoms onto the CNT sheet via sputtering; (iv) stacking a series of CNT-metal foils; (v) spark plasma sintering (SPS). CNT forest was synthesized via chemical vapor deposition (CVD) at 700 °C with C_2H_2 gas on a SiO_2/Si substrate. We obtained the forest from A-tech system Co., Korea. One edge of the CNT forest was drawn as a sheet form and attached onto a U-shaped holder. The suspended CNT sheet was transferred onto an Al foil (50 mm × 10 mm, thickness: 25, 38, 100 μm, Alfa Aesar, US). The metal (Al) deposition on CNT sheet was performed via sputtering (A-tech system Ltd., Korea) with 5 N Al target (Process Materials Inc., USA). The argon gas flow was 10 sccm, and the pressure was 1.3–1.4 mTorr with 160 W for 30 min. The Al-deposited CNT-Al foils were stacked repeatedly. The normal Al foil covered the top of the stacked CNT-Al foils (final thickness = 5 mm). The stacked Al–C foil was sintered using SPS equipment (Eltek Ltd., Korea) at optimized temperature condition (580 °C, Fig. S2 in Supporting Information) for 30 min with 560 kgf under vacuum (~10^{-2} Torr). The heating rate was 35 °C min^{-1}. Moreover, the sintered sample was heat treated at 500 °C for 60 min under Ar atmosphere. The average weight of a single layer of the as-pulled CNT sheet is 8 μg. The concentration of CNT is depended on the thickness of Al foil. In case of using 25 μm of Al foil which is the minimum manageable, the added number of CNT layers is 19, which is equivalent to 0.15 vol% (0.02 wt %) in the final composite (0.03 vol% at 100 μm, 0.10 vol% at 38 μm). Further details are given in the Supporting Information (Fig. S2). The controlled raw sample was also fabricated similarly without CNT sheets.

2.2. Characterization

The morphologies of each process were observed using field-emission scanning electron microscopy (FE-SEM, JEOL 7600F) and transmission electron microscope (TEM, TECNAI G2 F20 460L). For the TEM observation, the sample surface was polished using an auto polisher (MetPrep, Allied high tech products Inc.) with SiC papers (800, 1200 grit) and a polycrystalline diamond (3, 1 μm) suspension. The dimple was formed in the center of a sample by a dimpling machine (656 dimple grinder, Gatan Inc.) with

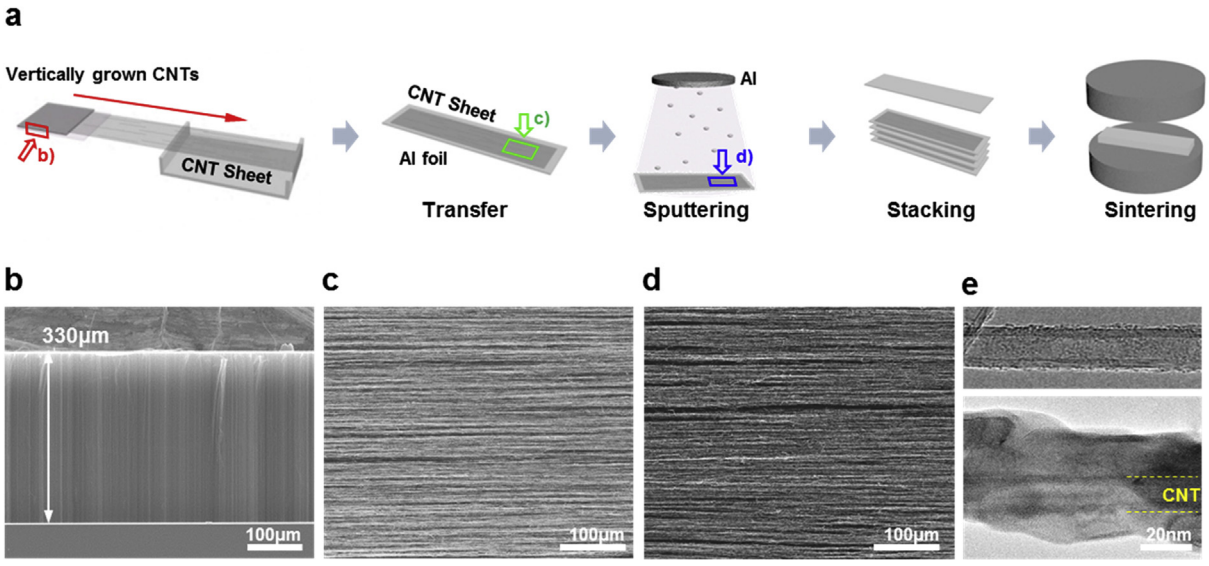

Fig. 1. Fabrication method and micrograph of CNTs and the composite. (a) Schematic illustration of the fabrication method of the metal-CNT composite. SEM image of (b) the cross-sectional view of the vertically grown CNTs and (c) top view of the as-pulled CNT sheet, (d) metal-deposited CNT sheet. (e) TEM image of the individual pristine CNT (top) and metal-deposited CNT (bottom). (A colour version of this figure can be viewed online.)

polycrystalline diamond (1 μm) suspensions. Finally, the dimpled sample was ion-milled using a precision ion polishing system (695 PIPS II, Gatan Inc.) until exposure of CNTs. The ion-polished sample was used in X-ray photoelectron spectroscopy (XPS, PREVAC) measurement. The structural changes were characterized using X-ray diffraction (XRD, Rotaflex D/MAX system, Rigaku) with Cu Kα radiation (λ = 1.54 Å). The alignment and structural changes of CNTs were measured using a confocal Raman microscope (NTEGRA spectra, NT-MDT) with a wavelength of 532 nm. The location of CNTs in the matrix was characterized using Raman mapping system (XperRam 200, Nanobase Ltd., Korea) with a wavelength of 532 nm. Prior to XRD and Raman measurement, the cross-section surface of the composite was prepared with the same polishing condition of the TEM sample. The tensile test specimens were tailored in the shape of a dog bone with the gage length of 2 mm and width of 1.5 mm. The mechanical properties were measured using a universal testing machine (LR10K, Lloyd, US, 4–5 times per sample). The strain rate was 0.2 mm min^{-1}. The elongation (strain) was measured by the machine extension owing to the small size of the specimen, and was then modified by the actual gaged extension of the tensile specimens. Further details are provided in the Supporting Information (Fig. S3).

3. Result

For the uniaxial alignment of CNTs in the metal matrix, we aligned CNTs along the pulling direction horizontally from the CNT forest using a mechanical pulling. The vertically grown CNT forest was synthesized via CVD. The average length of CNT was 330 μm, as confirmed using SEM in Fig. 1b. Fig. 1c and d shows the top view of the as-pulled CNT sheet and Al-deposited CNT sheet, respectively. The CNTs are superaligned along the pulled direction. The main driving force of the continuous pulling of the CNT sheet is the van der Waals interaction between the long CNTs [15,20]. After the deposition of Al, the CNT surface is covered with Al atoms. Owing to the thickness of the CNT sheet, a non-uniform Al deposition is observed between the top and bottom parts of the CNT sheet during Al sputtering. The TEM image in Fig. 1e reveals that the average CNT diameter changes from 15.3 nm (±1.3 standard deviation, SD) in the pristine CNT (upper image, Fig. S4 in Supporting Information) to 70 nm after Al deposition (lower image, it is from the bottom part of Al-deposited CNT sheet, Fig. S5 in Supporting Information). The diameter of the metal-deposited CNT is in the range of 50–180 nm. Nevertheless, Al atoms are deposited on the entire CNT surface.

Polarization-dependent Raman spectroscopy is used to investigate the degree of CNT alignment. In Fig. 2a, Φ = 0° when the polarization axis of input light coincides with the aligned axis of CNTs. The G-band intensity of CNTs near 1575 cm^{-1} decreases as Φ approaches 90° owing to the anisotropic absorption feature of CNTs. This indicates that the CNT sheet is superaligned along the pulled direction [21]. During the sputtering process, Al atoms are physically deposited onto the CNT surface [22], and consequently, the peaks of Al crystal are observed in the XRD patterns, as shown in

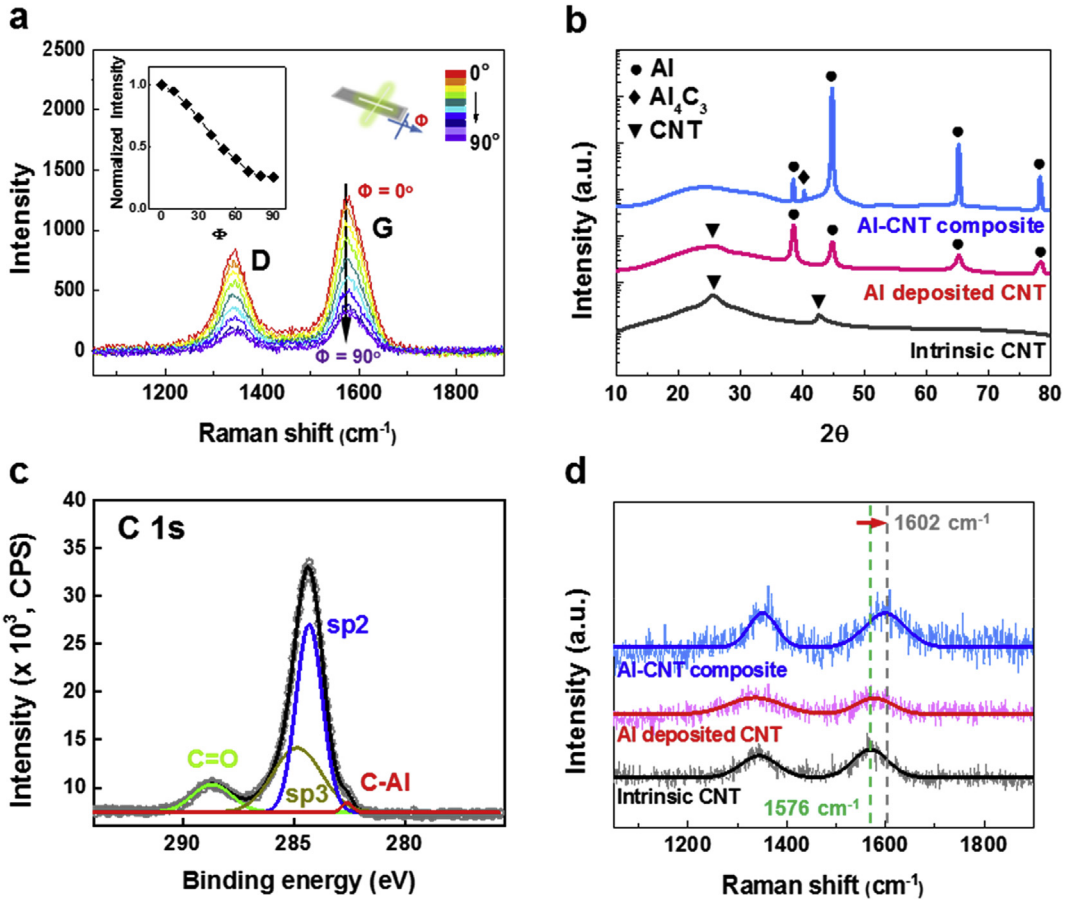

Fig. 2. Characterization of CNTs and the Al-CNT composite. (a) Polarization-angle dependent Raman spectra of the as-drawn CNT sheet with a step of 10°. Inset shows the angle dependence of G-band intensity. (b) XRD results for the intrinsic CNT sheet (black line), Al-deposited CNT sheet (magenta line), and Al-CNT composite (final product, blue line). Al, Al_4C_3, and CNT peaks are marked with a circle, rhombus, and inverted triangle symbols, respectively. (c) XPS patterns of C 1s peak of the Al-CNT composite. (d) Raman spectra for the same samples as XRD measurement. (A colour version of this figure can be viewed online.)

Fig. 2b. After sintering, the Al–C compound is formed, contributed by the reaction between the deposited Al atoms and CNTs. The signature of Al_4C_3 formation is marked with a rhombus symbol in the final product [16]. For unambiguous identification of crystal information of Al–C compound, we etched the Al-CNT composite using acidic solution until all of the Al matrices is removed. After filtering, although peaks corresponding to both Al_4C_3 and Al_2O_3 crystal structures appear (Fig. S6 in Supporting Information), this result indicates that the partially crystallized compounds are Al_4C_3 crystals because the Al_2O_3 comes from the oxidation of aluminum during the etching process. Also, the formation of Al–C compounds is also demonstrated via the X-ray photoelectron spectroscopy (XPS) measurement. Fig. 2c shows the XPS result of C 1s peak of Al-CNT composite. The peaks near 284.5 eV and 285.3 eV are associated with sp^2 (blue line) and sp^3 (dark yellow line) of carbon bonds in the CNT, respectively. The peak at 289.2 eV corresponds to the carbon-oxygen bonds (green line). The peak near 282.7 eV is assigned to the carbon-aluminum binding energy (282.4 eV) [23,24], which indicates the formation of an Al–C compound via inter-diffusion between them. The Al–C related peaks (74.5 eV) is also observed in Al 2p (Fig. S7, Supporting Information) [24]. The D/G intensity ratio of the CNTs increases from 0.75 in the pristine CNTs to 0.96 after sputtering, as shown in Fig. 2d. The CNTs are damaged by plasma during sputtering. This leads to the structural deformation of CNTs from sp^2 to sp^3, resulting in the development of the disordered carbon peak (D-peak, 1330 cm^{-1}) [22]. The formation of disordered carbon structures accelerates the formation of Al–C compound at the CNT surface during sintering. The D/G ratio is further increased to 1.02 owing to the formation of Al–C compound in the final product. The G-band peak is upshifted (1602 cm^{-1}) in the final sample compared with the pristine CNTs (1576 cm^{-1}). Since the interfacial chemical bonds lead to the charge transfers from the CNTs to Al [25] and the applying strain into the lattice of CNT owing to the lattice mismatch between CNT and Al–C compounds [26], the peak shift of G-band is observed after sintering [27,28]. Thus, this phenomenon also indicates the formation of Al–C chemical bonds.

The presence of CNTs in the final product is determined using Raman mapping and TEM observations. Fig. 3a shows the optical image of the cross-section of the Al-0.15 vol% CNT composite, which reveals the CNTs bundles separated from each other by approximately 20 μm, which is equivalent to the thickness of the Al foil (25 μm). The inset shows Raman spectroscopy images with G- and D-bands, which are noisy due to the embedded CNTs in the matrix. Fig. 3b shows the G-band mapping image (1520–1680 cm^{-1}) of the region contained within the green box in Fig. 3a. The high G-band intensity (red color) is consistent with the dark line in the optical image, which indicates the presence of CNTs. The CNTs were localized between Al foils. Fig. 3c shows that the aligned CNTs can be observed (Fig. S8, Supporting Information). In the high-resolution TEM image (Fig. 3d), tubular CNT morphology is distinguishable from that of the Al–C compound. The layered structure is visible in the inner phase, and the distance between the layer is 0.34 nm (Fig. 3e), corresponding to the interlayer distance between the CNT walls [29]. The high crystallinity of CNTs was also confirmed by the thermos-gravimetric analysis (TGA, Fig. S6 in Supporting Information) with the etching method. Although the burning temperature of CNTs in the filtered sample (near 560 °C) is a little bit lower than the pristine CNT's one (near 580 °C) because of some defects on CNT surface during process, it shows the similar oxidation tendencies, which indicate that the initial CNT structures (crystallinity) are still retained in the final process [30]. Furthermore, an amorphous phase and partial crystal structure are visible in the outer region. In the crystal region, the lattice distance is 0.21 nm, corresponding to the (0 1 8) plane of Al_4C_3 [26], as shown in Fig. 3f. During the formation of Al–C compound, the average diameter of CNTs was decreased to 14.5 nm (±1.2 SD) from 15.3 nm (±1.3 SD) of pristine CNTs (Fig. S9, Supporting Information). The difference between two CNTs diameters is 0.8 nm, which corresponds to the degradation of 1–2 CNTs walls. While the intrinsic

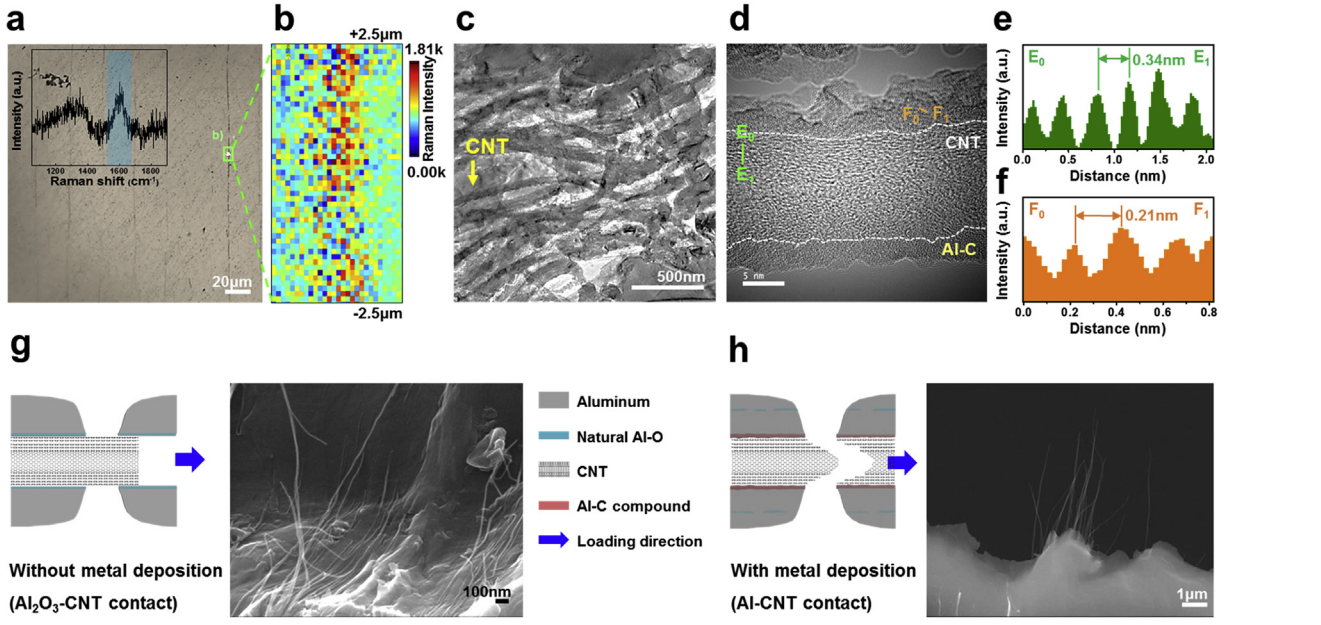

Fig. 3. Microstructure of the Al-0.15 vol% CNT composite. (a) Optical image of the cross-section of the composite. Black lines indicate the location of the CNTs. Inset shows the Raman spectrum. (b) Raman mapping image for scanning G-band intensity ranging from 1520 to 1680 cm^{-1}, inset in (a), for the selected area corresponding to the green dashed box in (a). Scan area is 5 μm × 2.5 μm. The red color indicates high intensity and the blue color indicates low intensity of G-band. TEM image of (c) the ion-milled final composite and (d) the individual CNT covered with the Al–C compound layer. Contrast line profile for lattice distance in (e) inner phase, (f) outer phase of (d). Average lattice distance of the inner phase is 0.34 nm and that of the outer phase is 0.21 nm. Illustration of interaction between Al and CNT under tensile stress and SEM image of the fracture surface after the tensile test; (g) without Al deposition and (h) with Al deposition. (A colour version of this figure can be viewed online.)

CNT comprises of 16 walls in average (Fig. S4, Supporting Information), most of the initial CNT structures are still retained.

Fig. 3g and h shows the fracture surfaces of Al-0.15 vol% CNT composite at iso-strain state after the tensile test without and with metal deposition via sputtering, respectively. Without sputtering, the natural oxide present on the Al foil surface prevents the formation of the Al–C compound and the CNTs simply slip from the Al matrix during the tensile test due to the weak bonds between the carbon atoms and Al matrix (Fig. S10a in Supporting Information). As a result, the prolonged CNTs with the clean surface were observed mainly in the slipped surface, as shown in Fig. 3g and Fig. S11a in Supporting Information. However, after Al deposition via sputtering, CNTs react with the deposited Al atoms, forming the Al–C compound quickly, leading to strong chemical bonding between the CNTs and matrix (Fig. S10b in Supporting Information). As a result, the CNTs with short lengths and sharp ends are mainly present in the fracture surface owing to the failure of CNTs (Fig. 3h and Fig. S11b in Supporting Information). The most compelling evidence for the strong bonding is short and protruded sharp ends of CNTs owing to the fractured CNT surface caused by the pull-out process [7,16].

The stress–strain curves of the raw Al and Al-0.15 vol% CNT composite (0°, iso-strain state) are illustrated in Fig. 4a. With the addition of 0.15 vol% superaligned CNTs, the Young's modulus, yield strength (0.2% off-set), and tensile strength of the composite are improved by 3.1%, 21.9%, and 20.1% on average, respectively. The improvement (ΔM) is defined by $(M_{composite} - M_{raw})/M_{raw} \times 100\%$, where M indicates the mechanical property. In contrast to the enhanced mechanical strengths, the elongation is reduced by 5.9%. The absolute and improvement values are listed in Table 1. The misorientation angle dependence of such mechanical properties of Al-0.15 vol% CNT composite is shown in Fig. 4b–e. The absolute values of mechanical properties shown in the upper panel do not reveal any insightful angular dependence. To assess the tendency of angle dependence, we analyzed the relative improvement (lower panel). The modulus and strengths decrease in proportion to the misorientation angle. In contrast to those tendencies, the change of improvement in elongation is not appreciable, regardless of the misorientation (Fig. 4e). The mechanical properties of various concentration of CNT are summarized in Fig. 5 and Figs. S12 and S13 (Supporting Information). The 0.1 vol% CNT composite has a similar anisotropic tendency of the 0.15 vol% CNT composite. On the other hand, the near-isotropic behavior is observed in 0.03 vol% CNT composite because the little concentration of CNT is not sufficient to affect the mechanical strength. A reduction in elongation is observed in all samples. Also, the degradation of elongation is increased in proportion to the concentration of CNTs, regardless of the misorientation angle. Further details are explained in the Discussion section.

4. Discussion

In the CNTs-reinforced MMCs, the various strengthening mechanisms had been suggested. Since the dispersed CNTs inhibit the dislocation propagation, the strength of the composite is improved, which can be explained using the Orowan looping. Moreover, the mismatch between the thermal expansion coefficients of the matrix and the CNTs generates dislocations in the metal matrix during the high-temperature process such as a heat treatment, sintering, and casting. The increased dislocation density within the matrix leads to the strengthening of the composite (generation of dislocations by the thermal mismatch) [16]. And the CNTs act as a fragmentation media of grains during the grain growth system because the CNTs influence the grain growth rate

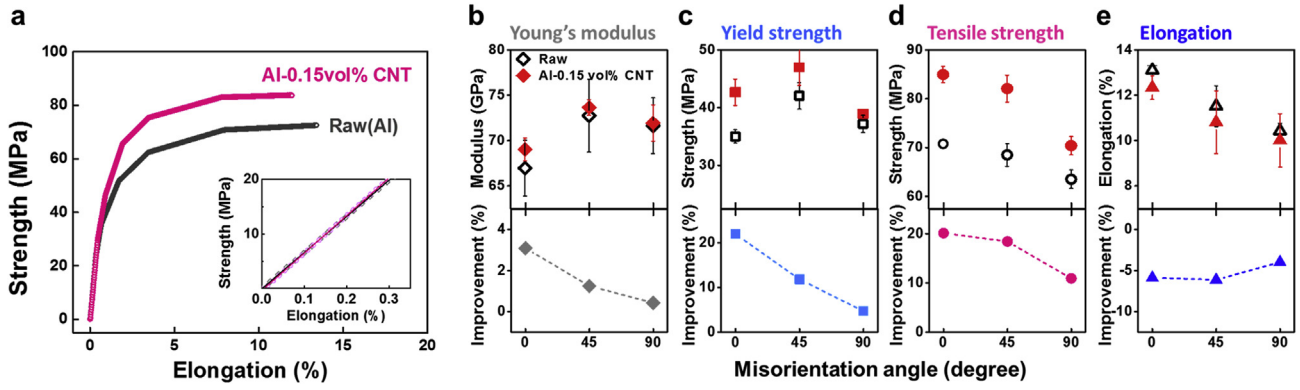

Fig. 4. Mechanical properties of raw Al and the Al-0.15 vol% CNT composite. (a) Stress-strain curve of the raw Al (black line) and Al-CNT composite (magenta line) in the iso-strain state (misorientation angle = 0°). The inset represents the elastic deformation region. Angular dependence of mechanical properties of Al-0.15 vol% CNT composite: (b) Young's modulus, (c) yield strength, (d) tensile strength, and (e) elongation. The upper panels represent the absolute values of mechanical properties. The raw Al and Al-CNT composite are marked with black open symbols and red solid symbols, respectively. The lower panels represent the relative improvement. The dotted lines are visual indications for the eyes. (A colour version of this figure can be viewed online.)

Table 1
Summary of the average mechanical properties of raw Al and Al-0.15 vol% CNT composites with angular dependence.

Misorientation angle [θ]		Young's modulus		Yield strength		Tensile strength		Elongation	
		[GPa]	Improvement [%]	[MPa]	Improvement [%]	[MPa]	Improvement [%]	[%]	Improvement [%]
0°	RAW	66.9		35.0		70.7		13.1	
	Al-CNT	69.0	3.1↑	42.7	21.9↑	84.9	20.1↑	12.3	−5.9↓
45°	RAW	72.7		42.0		68.5		11.5	
	Al-CNT	73.6	1.2↑	47.0	11.8↑	81.1	18.4↑	10.8	−6.1↓
90°	RAW	71.6		37.1		63.5		10.4	
	Al-CNT	71.9	0.4↑	38.9	4.7↑	70.4	10.9↑	10.0	−4.0↓

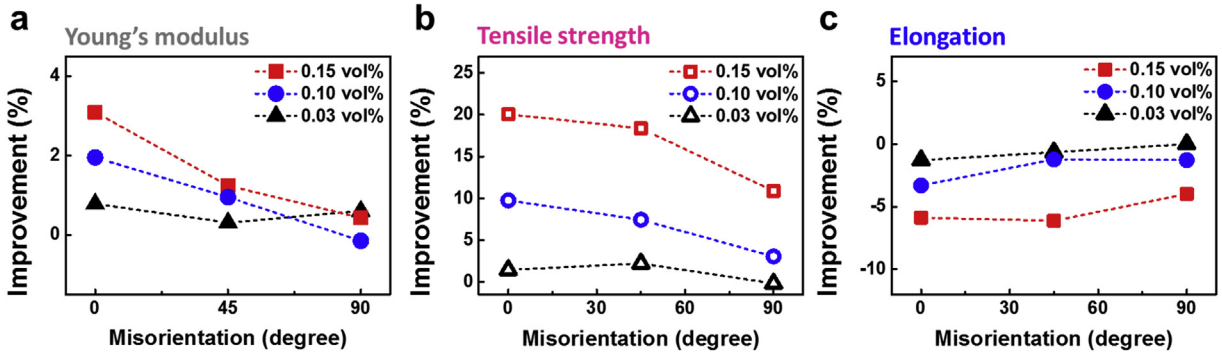

Fig. 5. Mechanical anisotropies of Al-CNT composite with various CNT concentration: (a) Young's modulus, (b) tensile strength, and (c) elongation. (A colour version of this figure can be viewed online.)

and hinder the dynamic recovery process of metal matrix, resulting in the grain refinement effect [31]. In addition, the applied stress is transferred into the strong CNTs through interfacial shear stress from the matrix, corresponding to the load transfer, which also improves the strength. These strengthening systems are believed to occur simultaneously. Thus, the multiple strengthening mechanisms, which are given by the sum of each improvement by the Orowan looping (OL), dislocation generation by thermal mismatch (TM), grain refinement (GR), and load transfer (LT), have been proposed as the prediction model for tensile strength of CNTs-reinforced MMCs as follows [11,16,32].

$$\sigma_C = \sigma_M + \Delta\sigma_{OL} + \Delta\sigma_{TM} + \Delta\sigma_{GR} + \Delta\sigma_{LT} \quad (1)$$

where $\Delta\sigma$ is the improvement of tensile strength by each of the mechanisms. Although the prediction model of anisotropic mechanical properties in 1D-reinforced composite with alignment is already well-established, there are few postulates. All reinforcements should be entirely bonded with the matrix, and the tensile load should be applied uniformly in an entire cross-section of specimen. Fortunately, in our sample, all CNTs were strongly bonded with the Al matrix owing to the Al deposition process and high-temperature reaction. Also, since the CNT sheets with a thickness of submicron were localized into the Al matrix (details are provided in Section 4.1) with the uniform intervals, the load was applied into the specimen homogeneously. However, owing to the unexpected non-linear structures of CNTs, we need to modify the conventional prediction model. And we used the measured average diameter of CNTs (D_{CNT} = 14.5 nm, Fig. S9 in Supporting Information) in the prediction model, taking into account the degradation of CNTs.

4.1. Strengthening effects

Among the various strengthening effects, three mechanisms – Orowan looping, dislocation generation, and grain refinement – are not related to the alignment angle of the CNTs, owing to their random occurrence [16,32]. We calculated each improvement in the tensile strength of the Al-0.15 vol% composite. The improvement of tensile strength owing to the Orowan looping system ($\Delta\sigma_{OL}$) can be calculated using Equation (2) [33].

$$\Delta\sigma_{OL} = \frac{0.13 G_M b}{\lambda'_{CNT}} \ln\frac{r_s}{b} \quad (2)$$

where G_M is the shear modulus of the matrix, which is defined as $G_M = E_M/2(1+\upsilon_M)$. Here, E_M is Young's modulus of the matrix (obtained from experimental data of the Al raw at iso-strain state, 66.9 GPa) and υ_M is the Poisson's ratio of the matrix (0.334). The calculated G_M is 25.0 GPa. Further, b is the Burgers vector of the matrix (b_{Al} = 0.286 nm), and r_S is the radius of a spherical reinforcement model (2.35×10^{-7} m). λ'_{CNT} is the effective inter-particle spacing (distance between face-to-face CNTs = 2.74×10^{-6} m). The detailed explanations are available in the previous report [16]. Thus, $\Delta\sigma_{OL}$ is 2.2 MPa (improved by 3.1% compared with the experimental data of Al raw at iso-strain). The improvement owing to the thermal mismatch mechanism ($\Delta\sigma_{TM}$) can be calculated using Equation (3) [33].

$$\Delta\sigma_{TM} = kG_M b\sqrt{\rho} \quad (3)$$

where k is a constant (1.25), and ρ is the enhanced dislocation density, which can be calculated as follows:

$$\rho = 12\frac{\Delta\alpha\Delta T V_{CNT}}{b d_R (1 - V_{CNT})} \quad (4)$$

where $\Delta\alpha$ is the difference between the thermal expansion coefficients of Al ($2.36 \times 10^{-5} K^{-1}$) and the CNTs ($2.1 \times 10^{-5} K^{-1}$) [34], ΔT is the difference between the temperatures of the heat treatment process (580 °C) and tensile testing (25 °C), and d_R is the diameter of the spherical reinforcement model ($d_R = 2r_S = 4.7 \times 10^{-7}$ m). The calculated ρ is 1.91×10^{11} m^{-2}, and the calculated value of improved strength is 2.18 MPa (improved by 3.1% compared with the experimental data of Al raw at iso-strain). In contrast to the conventional composite model with random dispersion of CNTs in the matrix (Fig. 6a), the CNTs are localized between the Al–Al foils in our study (Fig. 6b). Although the localized CNTs disturb the dislocation movement, the strengthening effects by both Orowan looping and dislocation generation by thermal mismatch locally occur around the CNT sheets only. Such localized enhancement effects do not affect the entire sample because the separation distance between each localized CNT sheet is very large (approximately 20 μm at the Al-0.15 vol% CNT composite, Fig. 3a). In the plastic deformation region, a strain hardening occurs owing to the interference of dislocations. The stress-strain relationship can be explained by a power law as follows [35].

$$\sigma_t = K\varepsilon_t^n \quad (5)$$

where σ_t is the true stress ($\sigma_t = \sigma(1+\varepsilon)$), ε_t is the true strain ($\varepsilon_t = \ln(1+\varepsilon)$). K is the strength coefficient and n is the work hardening exponent. K and n can be calculated by the logarithmic scale of stress-strain relationship ($\log\sigma_t = K + n\log\varepsilon_t$). The slope is equal to the n. Fig. 6c shows the work hardening exponents (n) of raw Al and Al-0.15 vol% CNT composite. The change in n is not noticeable,

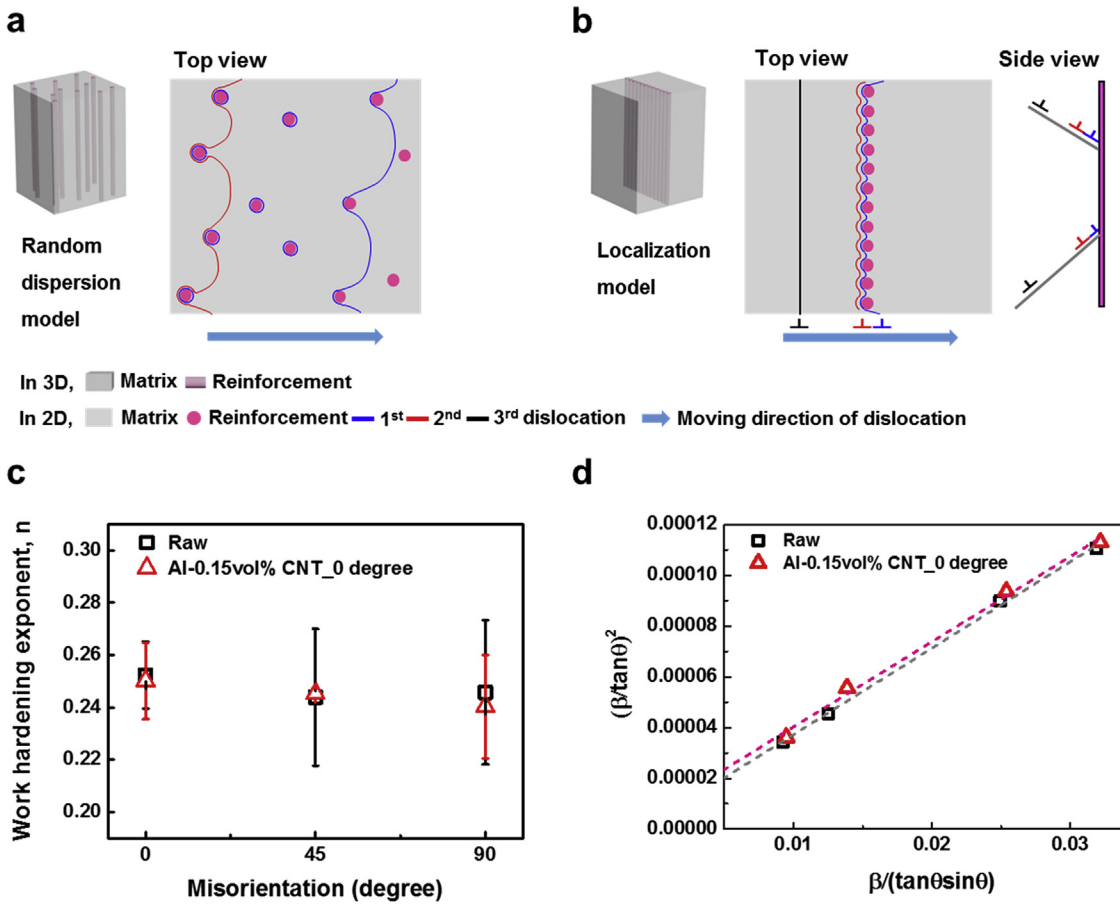

Fig. 6. Dispersion Models of the uniaxially aligned CNTs in the matrix. Schematic illustrations of (a) the random dispersion model associated with the conventional composite model and (b) localization model (our approach). The 2D images on the right are the top and side views of each model. (c) Work hardening exponent (n) of the Al-0.15 vol% CNT composites with angular dependence. (d) Halder–Wagner plot of raw Al and the Al-0.15 vol% CNT composite for the iso-strain case. The black open squares represent the controlled raw sample and the red open triangles represent the Al-CNT composites in the plots of (c) and (d). The straight dashed lines are obtained by linear regression analysis in (d). (A colour version of this figure can be viewed online.)

regardless of misorientation. Their difference ($\Delta n = n_{composite} - n_{raw})/n_{raw} \times 100\%$) is −0.9% at 0°, 0.6% at 45°, and −2.2% at 90° (Fig. S14 in Supporting Information), indicating that the localized CNTs cannot effectively disturb the dislocation movement.

The grain size can be estimated by the Halder–Wagner equation with the XRD data as follows [36].

$$\left(\frac{\beta}{\tan\theta}\right)^2 = \frac{K\lambda}{d}\cdot\frac{\beta}{\tan\theta\sin\theta} + 16\varepsilon^2 \quad (6)$$

where β is the integral breadth, θ is the Bragg angle, λ is the wavelength, and K is the dimensionless shape factor. d and ε are the crystal size and microstrain, respectively. Equation (6) is regarded as a straight line equation (y = ax + b). $y = (\beta/\tan\theta)^2$ is plotted against $x = \beta/(\tan\theta\sin\theta)$. Fig. 6d shows the Halder–Wagner plot of raw Al and the Al-0.15 vol% CNT composite for the iso-strain case. The corresponding XRD patterns are provided in Fig. S15 of the Supporting Information. The calculated crystal sizes of raw Al and the composite are 476 nm and 484 nm, respectively. The average grain sizes were determined again by the electron back scatter diffraction (EBSD) method. Despite the adding CNT, two average grain sizes are similar ($d_{raw} = 782$ nm, $d_{Al\text{-}CNT} = 764$ nm, Fig. S15 in Supporting Information). The difference in grain size between XRD and EBSD results comes from difference in the measured position and range. In addition, there is no positional gradient of grain sizes between the central position of the foil and the immediate side of localized CNT in Al-CNT composite. And owing to the sintering process, the thickness of the localized CNT region was reduced from a few microns to submicron. Details were provided in Supporting Information. Such XRD and EBSD results indicate that the grain refinement does not occur owing to the artificial localization structure and deformation-free process. The strengthening effect of grain refinement can be calculated by the Hall–Petch relationship (Equation (7)) as follows [37,38].

$$\sigma_y = \sigma_0 + k_y d^{-1/2} \quad (7)$$

where σ_y is the yield strength, σ_0 is the intrinsic stress resisting the dislocation motion, k_y is the stress intensity coefficient, and d is the grain size where we used XRD data. σ_0 (3 MPa in pure Al) and k_y (0.032 $MNm^{-3/2}$ in pure Al) [38,39] are material constants. The calculated yield strengths of raw Al and the composite are 49.4 MPa and 49.0 MPa, respectively. This negligible difference indicates that grain refinement was not induced by the addition of the CNTs. There is a difference between the calculated and experimental values of yield strength because we used the polished samples to perform XRD. Consequently, the enhancement of strength by the three mechanisms is negligible. Thus, we can explain the anisotropic mechanical properties of CNTs-reinforced MMCs by the load transfer mechanism, internal force dispersion, and failure mode without the strengthening mechanisms mentioned above.

4.2. Anisotropy of mechanical properties

In the elastic deformation region, variation in the misorientation angle leads to a change in the internal force dispersion between the matrix and reinforcement, which will nonlinearly modulate the applied tensile and shear stress (strain) in the CNTs [5]. Thus, the contributions of the longitudinal modulus ($E_{\|}$, $\theta = 0°$, iso-stress), transverse modulus ($E_{\perp}$, $\theta = 90°$, iso-strain), and shear modulus (G) vary with the change in the alignment angle. The angular dependence of the Young's modulus of the composite (E_C) can be calculated using Equation (8) [5].

$$E_x = E_{\|}\left[cos^4\theta + \frac{E_{\|}}{E_{\perp}}sin^4\theta + \frac{1}{4}\left(\frac{E_{\|}}{G_C} - 2\nu_C\right)sin^2 2\theta\right]^{-1} \quad (8)$$

where θ is the misorientation angle, G_C is the shear modulus of the composite, and ν_C is the Poisson's ratio of the composite. $E_{\|}$ and $E_{\perp}$ of a non-continuous 1D-reinforced composite can be predicted by the Halpin–Tsai equation as follows [40].

$$\frac{E_{\|}}{E_M} = \frac{1 + (2l/d)\eta_{\|}V_{CNT}}{1 - \eta_{\|}V_{CNT}} \quad (9)$$

and

$$\frac{E_{\perp}}{E_M} = \frac{1 + 2\eta_{\perp}V_{CNT}}{1 - \eta_{\perp}V_{CNT}} \quad (10)$$

where $\eta_{\|} = [(E_{CNT}/E_M)\text{-}1]/[(E_{CNT}/E_M)+2(l/d)]$ and $\eta_{\perp} = [(E_{CNT}/E_M)\text{-}1]/[(E_{CNT}/E_M)+2]$. E_{CNT}, l, and d represent the Young's modulus, length, and diameter of the CNTs, respectively. In the Al-0.15 vol% CNT composite, the calculated improvement in $E_{\|}$ is 1.87% compared with E_M, which is consistent with that calculated from the rule of mixtures (ROM, $E_{\|} = V_{CNT}E_{CNT} + V_M E_M$, $\Delta E = 1.87\%$). The calculated improvement in $E_{\perp}$ is 0.36%, which is similar to that calculated from the reversed ROM ($1/E_{\perp} = V_{CNT}E_{CNT} + V_M E_M$, $\Delta E = 0.14\%$). The reversed ROM can be used to calculate G_C. The shear modulus is defined as $G = E/2(1+\nu)$, where ν is Poisson's ratio ($\nu_{Al} = 0.334$, $\nu_{CNT} = 0.19$ [41]). Moreover, ν_C can be predicted by the ROM. Fig. 7a compares the calculated (by Equation (8), gray dashed line) and experimental (blue open rhombus symbols) improvement in the Young's modulus of the Al-0.15 vol% CNT composite. Although the experimental values are slightly higher than the calculated values owing to the error factor from the indirect measurement of elongation, their anisotropic tendencies are well-matched.

In the plastic deformation region, the failure of the composite is associated with the change in fracture mode with the misorientation angle of reinforcement. At zero misorientation angle, the fracture propagation is initiated at the 1D reinforcements fracture. At a finite misorientation angle, the fracture propagates along the direction of shear fracture of the matrix [5]. Therefore, the

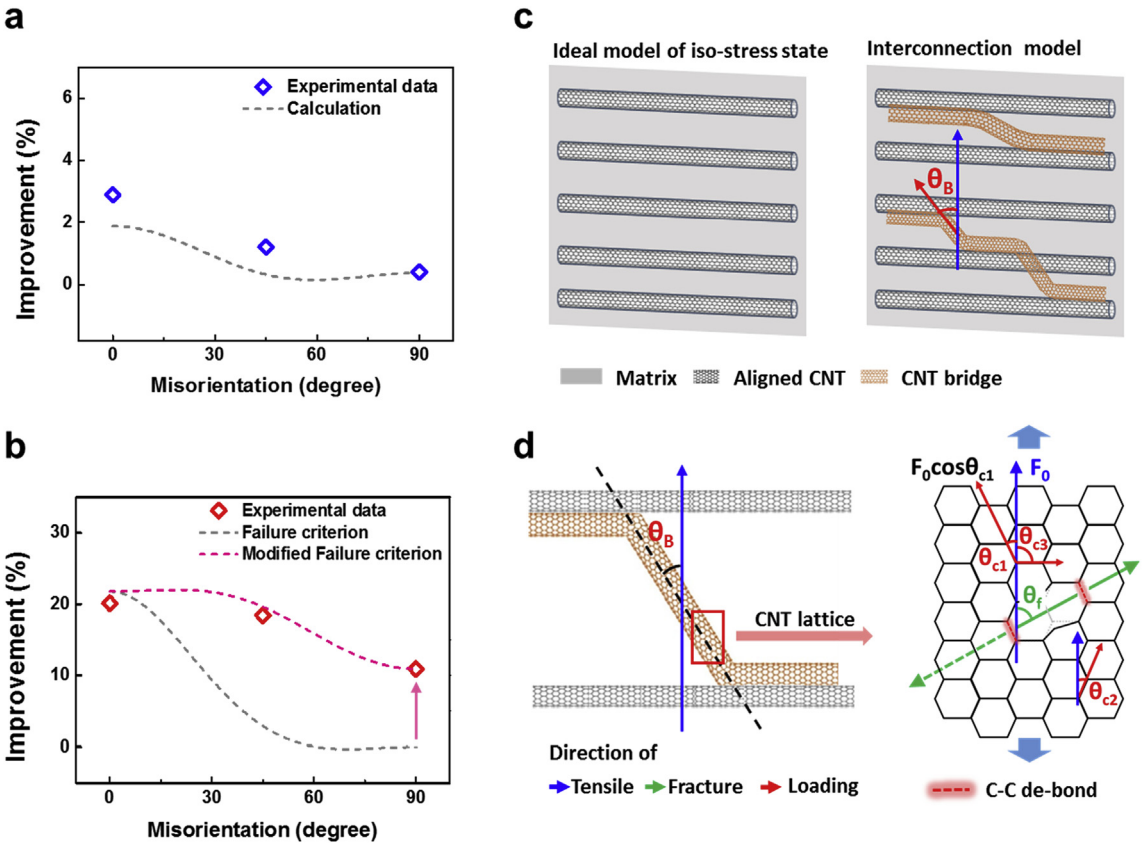

Fig. 7. Comparison of improvement in mechanical properties between calculation (dashed line) and experimental (open rhombus symbols): (a) Young's modulus, the calculated value (gray dashed line) was plotted using Equation (8). (b) tensile strength (gray and magenta dashed lines represent the data calculated by the failure criterion (Equation (11)) and modified failure criterion, respectively). Iso-stress state models of the Al-CNT composite. Schematics showing (c) the ideal model of the iso-stress state composite and interconnecting model, and (d) loading and fracture direction of hexagonal armchair CNT under the tensile test. The applied loading direction (red), fracture propagation direction (green), and tensile load direction (blue) are represented by arrows. θ_B is the misorientation angle of the CNT bridge, $\theta_{c1\text{-}3}$ are the applied loading angles, and θ_f is the fracture propagation angle. These are the tilt angles from the tensile load direction. (A colour version of this figure can be viewed online.)

contributions of the longitudinal tensile strength ($\sigma_{\parallel}$), transverse tensile strength ($\sigma_{\perp}$), and shear stress (τ) vary with the change in the alignment angle. The angular dependence of tensile strength can be predicted by the failure criterion as follows [12].

$$\sigma_x = \left[\frac{cos^4\theta}{{\sigma_{\parallel}}^2} + cos^2\theta sin^2\theta\left(\frac{1}{{\tau_M}^2} - \frac{1}{{\sigma_{\parallel}}^2}\right) + \frac{sin^4\theta}{{\sigma_{\perp}}^2}\right]^{-\frac{1}{2}} \quad (11)$$

where θ is the misorientation angle and τ_M is the shear strength of the matrix. Although CNTs were localized into Al matrix at uniform intervals (localized dispersion array), this failure criterion is applicable for our structure because the direction of fracture propagation does not change even if the degree of dispersion varies. Details are provided in the Supporting Information (Fig. S16). The strength of the non-continuous 1D-reinforced composite depends on the length of the reinforcement. The critical length (l_c) for effective load transfer is defined as $l_c = \sigma_{CNT}\, D_{CNT}/2\tau_M$ [42]. Here, σ_{CNT} is the tensile strength of the CNT (11 GPa) [1], D_{CNT} is the diameter of the CNT, and τ_M is the shear strength of the matrix ($\tau_M = 0.6 \times \sigma_M$) [43]. The calculated l_c is 1.96 μm. When $l \gg l_c$, $\sigma_{\parallel}$ can be calculated using Equation (12) [5].

$$\sigma_{\parallel} = \sigma_{CNT} V_{CNT} + (\sigma_M)_{\varepsilon^*_{CNT}} V_M \quad (12)$$

where $(\sigma_M)_{\varepsilon^*_{CNT}}$ is the maximum stress at the fracture strain of the CNTs ($\varepsilon^*_{CNT} = 9.9\%$, average strain in Ref. [1]). The calculated improvement of Al-0.15 vol% CNT composite is 21.8% compared with σ_M, which is consistent with the experimental result of 20.1% listed in Table 1. The small difference between the two values is ascribed to some defects in the real samples including the CNTs and/or Al matrix. Such near theoretical value is another evidence of the superaligned CNTs, ultra-high aspect ratio of CNTs, and strong bonds between the CNTs and Al matrix.

The strengthening effect by 1D reinforcements is minimal in the ideal iso-stress state. The fracture proceeds without any interference from the 1D reinforcements under the tensile load; hence, $\sigma_{\perp}$ is almost equal to σ_M, theoretically. Fig. 7b compares the calculated (by Equation (11), gray dashed line) and experimental (red open rhombus symbols) values of the tensile strength improvement of the Al-0.15 vol% CNT composite. There is a large difference between the two results. Unlike the ideal model, the aligned CNTs are connected to each other by the bent CNT referred to as the CNT bridge, which results in matrix fracture accompanied by the failure of the CNTs, as shown in the interconnecting model of Fig. 7c. Interaction between the aligned CNTs and CNT bridge is van der Waals, which is usually weak. However, during the high-temperature process, some atomic defects on the surface of CNTs created a cross-linked carbon structure on the connecting part [44]. Moreover, the Al–C compound was formed not only on the surface but also the connecting part, resulting in that the two CNTs shared the Al–C compound layer. Consequently, they strongly interacted by an interface sharing, which is demonstrated by the observation of pulled-out CNTs in the fracture surface of iso-stress state (Fig. S17, Supporting Information). As the applied load is directly transferred into the CNT bridges by the extension of the gap between the two aligned CNTs during the tensile test, additional energy is required in this model for failure of the CNTs. Consequently, the CNT bridges contribute to the strengthening effect. Changes in the misorientation angle (θ_B) between the CNT bridge and tensile load direction also modulate the strengthening efficiency. In addition, when considering the atomic structure, the CNT has three different loading angles ($\theta_{c\#}$, misorientation between the C–C bond direction and tensile load direction) owing to its hexagonal lattice structure, which leads to three different possible positions of the C–C de-bond under tensile load. For example, armchair CNT has loading angles of 30° (θ_{c1}), 30° (θ_{c2}), and 90° (θ_{c3}; red lines in the image on the right in Fig. 7d). Owing to the force distribution, the applied loads ($F_{c\#}$) for each loading angle change to $F_0 cos\theta_{c\#}$, where F_0 is the initial tensile load. The C–C de-bond should also be formed at the relatively lowest loading angle part (red dashed line with highlights). Thus, the fracture propagation angle (θ_f) of the CNT bridge is determined by the misorientation angle (θ_B) of the bridge. As CNT fracture propagates along the circumference of the outermost layer of CNTs [1,45], we can calculate the number of C–C de-bonds ($n_{c\text{-}c}$) and the relative required force for breaking the CNTs. Information on the armchair and zigzag CNTs with the angle dependence is provided in Figs. S18 and S19, and summarized in Tables S3 and S4. Note, however, the following: Even if one loading angle ($\theta_{c\#}$) smaller than another, the number of C–C de-bonds ($n_{c\text{-}c}$) can be relatively greater than the other (e.g., the 90° tilted armchair CNT and 45° tilted zigzag CNT in Figs. S18 and S19). Therefore, we have to consider both – the number of C–C de-bonds ($n_{c\text{-}c}$) and applied loads ($F_{c\#}$). As a result, the zigzag CNT at $\theta_B = 0°$ requires the relatively lowest force, and the armchair CNT at $\theta_B = 90°$ requires the relatively highest force for CNT failure. The ratio (α) between the highest and lowest value of the required force is 2.16. From this selection rule of CNT failure, we can deduce the volume fraction of the CNT bridge (V_{CB}). The applied load is directly transferred into the CNT bridges; hence, the tensile strength of the CNT bridge-reinforced part can be calculated by Equation (12) on replacing V_{CNT} with V_{CB}. If we assume that the tensile strength of the zigzag CNT is equal to σ_{CNT}, the minimum tensile strength of the CNT bridge-reinforced part is calculated by $\sigma_{min} = \sigma_{CNT} V_{CB} + (\sigma_M)_{\varepsilon^*CNT}(1\text{-}V_{CB})$, and the maximum is calculated by $\sigma_{max} = \alpha\sigma_{CNT}V_{CB} + (\sigma_M)_{\varepsilon^*CNT}(1\text{-}V_{CB})$. Moreover, as the average tensile strength ($\sigma_{aver.}$) of a randomly oriented 1D composite can be predicted by $\sigma_{aver.} = (\sigma_{max}\cdot\sigma_{min})^{1/2}$ [46,47], the calculated V_{CB} is 0.00045 for the 0.15 vol% CNT composite (0.00032 for the 0.1 vol% CNT composite) when assuming $\sigma_{aver.} = \sigma_{\perp}$ (experimental result). The calculation details are provided in the Supporting Information. The CNT bridges account for approximately 30% of the total CNTs. However, this does not imply that 30% of the CNTs are misaligned, but that there are many bent sections in the aligned CNTs, as proved by the agreement between the experimental and theoretical values in the iso-strain state ($\sigma_{\parallel}$).

Similar to the iso-strain state, fracture of the composite with $\theta = 45°$ occurs along the direction of shear fracture of the metal matrix owing to the weakest link phenomenon in the traditional theory. As a result, the tensile strength ($\sigma_{/\!/}$) is regarded as the matrix shear strength (τ_M). On the other hand, in our model, the matrix shear fracture (τ_M) and CNT tensile failure (σ_{CNT}) coincide because of the strengthening effect of the CNT bridge. Therefore, $\sigma_{/\!/}$ can be calculated by the ROM ($\sigma_{/\!/} = \tau_M(1\text{-}V_{CB}) + \sigma_{CNT}V_{CB}$), and the average of $\sigma_{/\!/}$ can be computed using the same process as described in the preceding paragraph with the calculated V_{CB}. The calculated improvement at $\theta = 45°$ is 19.4%, which is consistent with the experimental result of 18.4%. The calculation details are provided in the Supporting Information. The magenta dashed line in Fig. 7b represents the modified failure criterion of the 0.15 vol% CNT composite, which is based on Equation (11) by applying the measured $\sigma_{\perp}$ and replacing τ_M with the calculated average $\sigma_{/\!/}$. The plotted result is very different from that of the normal failure criterion (gray dashed line), but is well-matched with the experimental results. The experimental tendencies of the 0.1 vol% CNT composite also match with the modified failure criterion, as described in the Supporting Information (Fig. S20).

In contrast to the anisotropies of strength and modulus, Fig. 5c reveals the near-isotropic behavior of elongation. A reduction in elongation is observed in the CNTs-reinforced composite owing to

the lower elongation of CNTs [1] than the matrix and different Poisson's ratios of the matrix, Al–C compound, and CNTs [1], which act as a defect site (Fig. S21, Supporting Information). The change of improvement in elongation is not appreciable, regardless of the misorientation due to the constant defect density. The defect density is proportional to the CNT concentration. Thus, the degradation of elongation is increased in proportion to the concentration of CNTs.

4.3. Strengthening efficiency

Fig. 8a shows the comparison between theoretical and experimental values of improvement of tensile strength with various concentration under the iso-strain state. The calculated tensile strength is given by $\sigma_C = \sigma_M$ (1-V_{CNT}) when the volume fraction of CNT is tiny, that is below the critical volume fraction (V_{crit}) as follows [5].

$$V_{crit} = \frac{\sigma_M - (\sigma_M)_{\varepsilon^*_{CNT}}}{\sigma_{CNT} - (\sigma_M)_{\varepsilon^*_{CNT}}} \quad (13)$$

Due to the superb mechanical strength of CNT, the V_{crit} is only 0.015 vol%. In the case of $V_{CNT} > V_{crit}$, the theoretical values calculated by Equation (12) (red dashed line). Although small deviations are observed between them, their tendencies are well-matched. We note that, although only 0.1, 0.15 vol% CNTs are reinforced in the matrix, the mechanical properties are remarkably enhanced. The strengthening efficiency (R_W) is defined as $R_W = [(\sigma_C - \sigma_M)/\sigma_M]/W_{CNT}$, where W_{CNT} is the weight fraction of reinforcement [48,49]. Since, in the previous studies, the volume fractions were converted using their specific densities of CNT, we use the weight fraction to make a fair comparison. The strengthening efficiency and elongation changes ($\Delta\varepsilon$) of our composites are summarized in Fig. 8b, in comparison with the previous studies on Al-CNT composites [3,7,8,10,14,16,50–59] (the absolute values, fabrication process, and aspect ratio are listed in Table S5, Supporting Information). Our composite exhibits R_W of ~1000 in the iso-strain state, which is significantly higher than the previous values of 10–120 (orange box in Fig. 8b). Since the dispersion of CNTs is usually performed via ball milling process, the aspect ratio and crystallinity of CNTs are decreased [59,60]. Consequently, the strengthening effect of CNTs is significantly reduced in previous method. Our process directly applies the pulling method of superaligned CNTs and excludes the origin of physical damage. The strengthening effect is maximized and is close to the theoretical value. The elongation change ($\Delta\varepsilon$) obtained is − 5.9% in the iso-strain state with the adding 0.15 vol% CNTs, which is not noticeable compared with previous composites. Despite high strengthening efficiency, the low concentration of CNTs limits the proliferation of our approach into a real industry. As mentioned above, the manageable limitation of thin foil is critical bottle-neck in our approach, which needs to be improved further. The thinnest foil on the commercial market is 1 μm. The concentration of CNT will be able to reach to 3.8 vol% when using 1 μm Al foil (Fig. S22, Supporting Information). In addition, if all matrix metal is fully constructed by the deposition process, the range of possible CNT concentrations can be extended. Therefore, the combining between the full-deposition approach for matrix and our alignment method is a promising technique for the advanced CNT-reinforced metal matrix composite.

5. Conclusion

We reported the anisotropy of mechanical properties and their strengthening mechanisms in a CNT-reinforced Al matrix composite. The randomly generated strengthening effects such as Orowan looping, dislocation generation, grain refinement were artificially controlled by the localization of CNTs, to thereby demonstrate the influence of the alignment direction of the CNTs and their strengthening mechanism. The uniaxially aligned CNTs were obtained via the mechanical pulling method from a vertically grown CNT forest. The metal deposition process led to the strong bond between the metal matrix and CNTs. In addition, the ultra-high aspect ratio of CNTs was retained in the final product owing to the damage-free process used herein. Consequently, the mechanical properties were significantly enhanced and were achieved the near theoretical values in the iso-strain state, resulting in that the strengthening efficiency of Al-0.15 vol% CNT composite was ~1,000, which is one order of magnitude larger than those achieved in the previous works. Moreover, as the CNT bridges contributed to the strengthening effect, the tensile strength increased for not only the 45°-oriented composite but also the iso-stress state of the composite. The interconnecting model with the modified failure criterion explained these unusual mechanical anisotropies and their strengthening mechanisms. We believe that our suggested

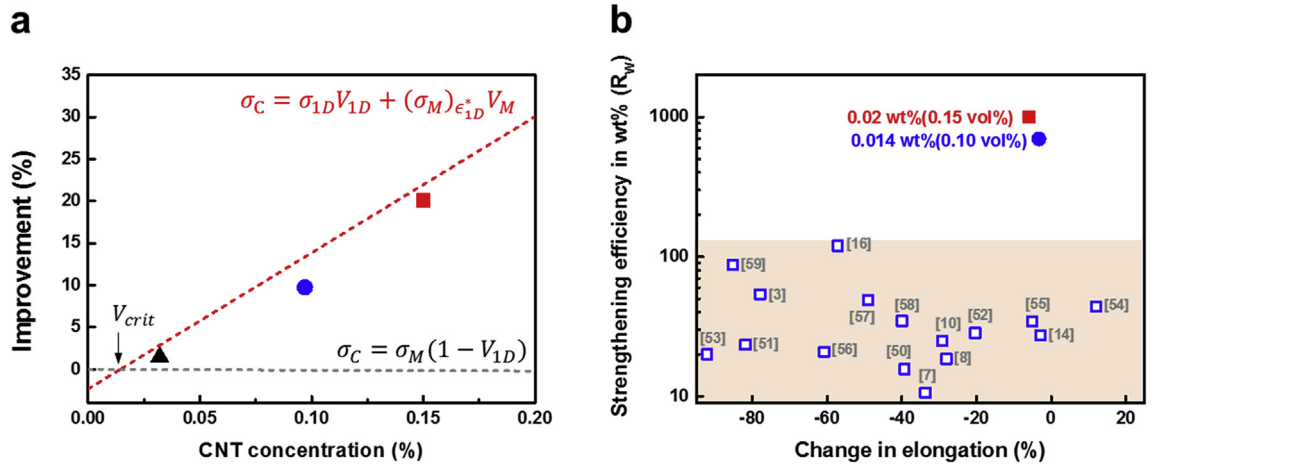

Fig. 8. Tensile strength and strengthening efficiency of the Al-CNT composite. (a) Comparison of calculated (dashed lines) and experimental (symbols) values of tensile strength. (b) Summary of strengthening efficiency (R_W) versus elongation change of the Al-CNT composite. The results of previous studies are represented by open blue square symbols with reference numbers and our results are represented by solid red square and blue circle symbols. Data range of previous studies is indicated in the orange box. (A colour version of this figure can be viewed online.)

alignment approach and prediction model for the anisotropic mechanical properties can contribute to advancement in the science and engineering of CNT-reinforced composites.

Acknowledgments

This work was supported by the Institute for Basic Science of Korea (IBS-R011-D1).

Appendix A. Supplementary data

Supplementary data to this article can be found online at https://doi.org/10.1016/j.carbon.2019.07.035.

References

[1] M.F. Yu, O. Lourie, M.J. Dyer, K. Moloni, T.F. Kelly, R.S. Ruoff, Strength and breaking mechanism of multiwalled carbon nanotubes under tensile load, Science 287 (5453) (2000) 637–640.
[2] K.P. So, X. Liu, H. Mori, A. Kushima, J.G. Park, H.S. Kim, S. Ogata, Y.H. Lee, J. Li, Ton-scale metal–carbon nanotube composite: the mechanism of strengthening while retaining tensile ductility, Extreme Mechanics Letters 8 (2016) 245–250.
[3] X.D. Yang, T.C. Zou, C.S. Shi, E.Z. Liu, C.N. He, N.Q. Zhao, Effect of carbon nanotube (CNT) content on the properties of in-situ synthesis CNT reinforced Al composites, Mat Sci Eng a-Struct 660 (2016) 11–18.
[4] H. Kwon, M. Estili, K. Takagi, T. Miyazaki, A. Kawasaki, Combination of hot extrusion and spark plasma sintering for producing carbon nanotube reinforced aluminum matrix composites, Carbon 47 (3) (2009) 570–577.
[5] B.D. Agarwal, L.J. Broutman, K. Chandrashekhara, Analysis and Performance of Fiber Composites, John Wiley & Sons, 2006.
[6] A. Kelly, G.J. Davies, The principles of the fiber reinforcement of metals, Metall. Rev. 10 (1965).
[7] A.M.K. Esawi, K. Morsi, A. Sayed, A.A. Gawad, P. Borah, Fabrication and properties of dispersed carbon nanotube–aluminum composites, Mater. Sci. Eng. A 508 (1–2) (2009) 167–173.
[8] A.M.K. Esawi, M.A. El Borady, Carbon nanotube-reinforced aluminium strips, Compos. Sci. Technol. 68 (2) (2008) 486–492.
[9] B.S. Guo, M. Song, J.H. Yi, S. Ni, T. Shen, Y. Du, Improving the mechanical properties of carbon nanotubes reinforced pure aluminum matrix composites by achieving non-equilibrium interface, Mater. Des. 120 (2017) 56–65.
[10] T.B. He, X.L. He, P.J. Tang, D.S. Chu, X.Y. Wang, P.Y. Li, The use of cryogenic milling to prepare high performance Al2009 matrix composites with dispersive carbon nanotubes, Mater. Des. 114 (2017) 373–382.
[11] F. Ogawa, C. Masuda, Microstructure evolution during fabrication and microstructure–property relationships in vapour-grown carbon nanofibre-reinforced aluminium matrix composites fabricated via powder metallurgy, Compos. Appl. Sci. Manuf. 71 (2015) 84–94.
[12] T.H. Courtney, Mechanical Behavior of Materials, Waveland Pr Inc, 2005.
[13] Z.Y. Liu, B.L. Xiao, W.G. Wang, Z.Y. Ma, Effect of carbon nanotube orientation on mechanical properties and thermal expansion coefficient of carbon nanotube-reinforced aluminum matrix composites, Acta Metall. Sin. 27 (5) (2014) 901–908.
[14] J.Z. Liao, M.J. Tan, I. Sridhar, Spark plasma sintered multi-wall carbon nanotube reinforced aluminum matrix composites, Mater. Des. 31 (2010) S96–S100.
[15] M. Zhang, S. Fang, A.A. Zakhidov, S.B. Lee, A.E. Aliev, C.D. Williams, K.R. Atkinson, R.H. Baughman, Strong, transparent, multifunctional, carbon nanotube sheets, Science 309 (5738) (2005) 1215–1219.
[16] J.G. Park, D.H. Keum, Y.H. Lee, Strengthening mechanisms in carbon nanotube-reinforced aluminum composites, Carbon 95 (2015) 690–698.
[17] C. Muratore, A.N. Reed, J.E. Bultman, S. Ganguli, B.A. Cola, A.A. Voevodin, Nanoparticle decoration of carbon nanotubes by sputtering, Carbon 57 (2013) 274–281.
[18] D. Lahiri, S.R. Bakshi, A.K. Keshri, Y. Liu, A. Agarwal, Dual strengthening mechanisms induced by carbon nanotubes in roll bonded aluminum composites, Mater. Sci. Eng. A 523 (1–2) (2009) 263–270.
[19] Y.-H. Li, W. Housten, Y. Zhao, Y.Q. Zhu, Cu/single-walled carbon nanotube laminate composites fabricated by cold rolling and annealing, Nanotechnology 18 (20) (2007) 205607.
[20] A.A. Kuznetsov, A.F. Fonseca, R.H. Baughman, A.A. Zakhidov, Structural model for dry-drawing of sheets and yarns from carbon nanotube forests, ACS Nano 5 (2) (2011) 985–993.
[21] G.S. Duesberg, I. Loa, M. Burghard, K. Syassen, S. Roth, Polarized Raman spectroscopy on isolated single-wall carbon nanotubes, Phys. Rev. Lett. 85 (25) (2000) 5436–5439.
[22] A. Gohel, K.C. Chin, Y.W. Zhu, C.H. Sow, A.T.S. Wee, Field emission properties of N2 and Ar plasma-treated multi-wall carbon nanotubes, Carbon 43 (12) (2005) 2530–2535.
[23] C.-D. Kim, H.T. Kim, Direct formation of graphene shells on Al 2 O 3 nanoparticles using simple thermal treatment under C 2 H 2 -H 2 atmospheric conditions, Mater. Chem. Phys. 202 (2017) 215–219.
[24] C. Hinnen, D. Imbert, J.M. Siffre, P. Marcus, An in situ XPS study of sputter-deposited aluminium thin films on graphite, Appl. Surf. Sci. 78 (1994) 219–231.
[25] K.P. So, C. Biswas, S.C. Lim, K.H. An, Y.H. Lee, Electroplating formation of Al–C covalent bonds on multiwalled carbon nanotubes, Synth. Met. 161 (3–4) (2011) 208–212.
[26] S.R. Bakshi, A.K. Keshri, V. Singh, S. Seal, A. Agarwal, Interface in carbon nanotube reinforced aluminum silicon composites: thermodynamic analysis and experimental verification, J. Alloy. Comp. 481 (1–2) (2009) 207–213.
[27] L.S. Schadler, S.C. Giannaris, P.M. Ajayan, Load transfer in carbon nanotube epoxy composites, Appl. Phys. Lett. 73 (26) (1998) 3842–3844.
[28] J.Z. Liao, M.J. Tan, R.V. Ramanujan, S. Shukla, Carbon nanotube evolution in aluminum matrix during composite fabrication process, Mater. Sci. Forum 690 (2011) 294–297.
[29] S. Iijima, Helical microtubules of graphitic carbon, Nature 354 (1991) 56–58.
[30] D. Bom, R. Andrews, D. Jacques, J. Anthony, B. Chen, M.S. Meier, J.P. Selegue, Thermogravimetric analysis of the oxidation of multiwalled carbon nanotubes: evidence for the role of defect sites in carbon nanotube chemistry, Nano Lett. 2 (6) (2002) 615–619.
[31] H. Zare, M. Jahedi, M.R. Toroghinejad, M. Meratian, M. Knezevic, Compressive, shear, and fracture behavior of CNT reinforced Al matrix composites manufactured by severe plastic deformation, Mater. Des. 106 (2016) 112–119.
[32] R. George, K.T. Kashyap, R. Rahul, S. Yamdagni, Strengthening in carbon nanotube/aluminium (CNT/Al) composites, Scr. Mater. 53 (10) (2005) 1159–1163.
[33] Z. Zhang, D. Chen, Consideration of Orowan strengthening effect in particulate-reinforced metal matrix nanocomposites: a model for predicting their yield strength, Scr. Mater. 54 (7) (2006) 1321–1326.
[34] L. Deng, R.J. Young, I.A. Kinloch, R. Sun, G. Zhang, L. Noé, M. Monthioux, Coefficient of thermal expansion of carbon nanotubes measured by Raman spectroscopy, Appl. Phys. Lett. 104 (5) (2014), 051907.
[35] H.J. KLEEMOLA, M.A. NIEMINEN, On the strain-hardening parameters of metals, METALLURGICAL TRANSACTIONS 5 (1974) 1863–1866.
[36] N.C. Halder, C.N.J. Wagner, Separation of particle size and lattice strain in integral breadth measurements, Acta Crystallogr. 20 (2) (1966) 312–313.
[37] E. HALL, The deformation and ageing of mild steel: III discussion of results, Proc. Phys. Soc. Sect. B 64 (1951) 747–753.
[38] J.W. Wyrzykowski, M.W. Grabski, The Hall–Petch relation in aluminium and its dependence on the grain boundary structure, Philos. Mag. A 53 (4) (1986) 505–520.
[39] J.T. Al-haidary, N.J. Petch, E.R. de los Rios, The plastic deformation of polycrystals I. Aluminium between room temperature and 400°C, Philos. Mag. A 47 (6) (1983) 869–890.
[40] J.C. HALPIN, J.L. KARDOS, The halpin-tsai equations: a review, Polym. Eng. Sci. 16 (1976) 344–352.
[41] A. Pantano, M.C. Boyce, D.M. Parks, Mechanics of axial compression of single and multi-wall carbon nanotubes, J Eng Mater-T Asme 126 (3) (2004) 279–284.
[42] S.R. Bakshi, A. Agarwal, An analysis of the factors affecting strengthening in carbon nanotube reinforced aluminum composites, Carbon 49 (2) (2011) 533–544.
[43] W.F. Smith, Structure and Properties of Engineering Alloys, McGraw-Hill, 1993.
[44] S. Zhang, A. Hao, N. Nguyen, A. Oluwalowo, Z. Liu, Y. Dessureault, J.G. Park, R. Liang, Carbon nanotube/carbon composite fiber with improved strength and electrical conductivity via interface engineering, Carbon 144 (2019) 628–638.
[45] B.I. Yakobson, M.P. Campbell, C.J. Brabec, J. Bernholc, High strain rate fracture and C-chain unraveling in carbon nanotubes, Computafional Materials Science 8 (1997) 341–348.
[46] M. Horio, S. Onogi, Dynamic measurements of physical properties of pulp and paper by audiofrequency sound, J. Appl. Phys. 22 (7) (1951) 971–977.
[47] R.E. LAVENGOOD, Strength of short-fiber reinforced composites, Polym. Eng. Sci. (1972) 48–52.
[48] S.I. Cha, K.T. Kim, S.N. Arshad, C.B. Mo, S.H. Hong, Extraordinary strengthening effect of carbon nanotubes in metal-matrix nanocomposites processed by molecular-level mixing, Adv. Mater. 17 (11) (2005) 1377–1381.
[49] L. Jiang, Z.Q. Li, G.L. Fan, L.L. Cao, D. Zhang, Strong and ductile carbon nanotube/aluminum bulk nanolaminated composites with two-dimensional alignment of carbon nanotubes, Scr. Mater. 66 (6) (2012) 331–334.
[50] K.P. So, J.C. Jeong, J.G. Park, H.K. Park, Y.H. Choi, D.H. Noh, D.H. Keum, H.Y. Jeong, C. Biswas, C.H. Hong, Y.H. Lee, SiC formation on carbon nanotube surface for improving wettability with aluminum, Compos. Sci. Technol. 74 (2013) 6–13.
[51] C.F. Deng, X.X. Zhang, D.Z. Wang, Q. Lin, A.B. Li, Preparation and characterization of carbon nanotubes/aluminum matrix composites, Mater. Lett. 61 (8–9) (2007) 1725–1728.
[52] R. Pérez-Bustamante, C.D. Gómez-Esparza, I. Estrada-Guel, M. Miki-Yoshida, L. Licea-Jiménez, S.A. Pérez-García, R. Martínez-Sánchez, Microstructural and mechanical characterization of Al–MWCNT composites produced by mechanical milling, Mater. Sci. Eng. A 502 (1–2) (2009) 159–163.
[53] C.N. He, N.Q. Zhao, C.S. Shi, S.Z. Song, Mechanical properties and microstructures of carbon nanotube-reinforced Al matrix composite fabricated by in

situ chemical vapor deposition, J. Alloy. Comp. 487 (1–2) (2009) 258–262.
[54] I. Sridhar, K.R. Narayanan, Processing and characterization of MWCNT reinforced aluminum matrix composites, J. Mater. Sci. 44 (7) (2009) 1750–1756.
[55] C.F. Deng, D.Z. Wang, X.X. Zhang, A.B. Li, Processing and properties of carbon nanotubes reinforced aluminum composites, Mat Sci Eng a-Struct 444 (1–2) (2007) 138–145.
[56] R. Xu, Z. Tan, D. Xiong, G. Fan, Q. Guo, J. Zhang, Y. Su, Z. Li, D. Zhang, Balanced strength and ductility in CNT/Al composites achieved by flake powder metallurgy via shift-speed ball milling, Compos. Appl. Sci. Manuf. 96 (2017) 57–66.
[57] M.T.Z. Hassan, A.M.K. Esawi, S. Metwalli, Effect of carbon nanotube damage on the mechanical properties of aluminium–carbon nanotube composites, J. Alloy. Comp. 607 (2014) 215–222.
[58] Z.Y. Liu, S.J. Xu, B.L. Xiao, P. Xue, W.G. Wang, Z.Y. Ma, Effect of ball-milling time on mechanical properties of carbon nanotubes reinforced aluminum matrix composites, Compos Part a-Appl S 43 (12) (2012) 2161–2168.
[59] C.R. Bradbury, J.K. Gomon, L. Kollo, H. Kwon, M. Leparoux, Hardness of multi wall carbon nanotubes reinforced aluminium matrix composites, J. Alloy. Comp. 585 (2014) 362–367.
[60] D. Poirier, R. Gauvin, R.A.L. Drew, Structural characterization of a mechanically milled carbon nanotube/aluminum mixture, Compos. Appl. Sci. Manuf. 40 (9) (2009) 1482–1489.

Anisotropic mechanical properties and strengthening mechanism in superaligned carbon nanotubes-reinforced aluminum

*Jong Gil Park, Jeong-Gyun Kim, Kang Pyo So, Jun Yeon Hwang, Eun Sung Kim, Ju Li, Dongseok Suh, Young Hee Lee**

- **Concept of 1-dimensional-material-reinforced composite**

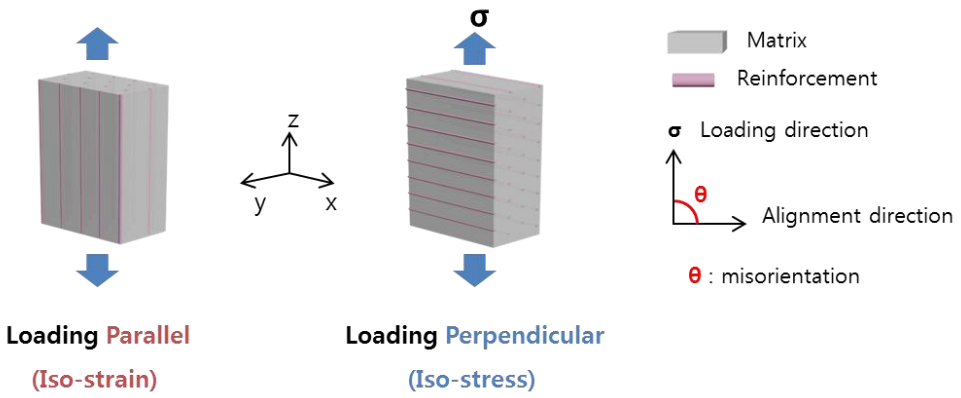

Figure S1. Schematic illustrations of the one-dimensional (1D)-material-reinforced composite under tensile stress with the alignment angle of reinforcement. In the left, the 1D reinforced material is aligned in parallel with the loading direction (θ = 0°, iso-strain state). In the right, the 1D reinforced material is aligned perpendicular to the loading direction (θ = 90°, iso-stress state). Here, θ is a misorientation angle between the alignment direction of 1D reinforcement and the loading direction.

- **Fabrication method**

A carbon nanotube (CNT) forest was synthesized via chemical vapor deposition. One edge of the CNT forest was drawn as a sheet form and attached onto a U-shaped holder, as shown in Figure S2 a. The suspended CNT sheet was transferred onto an Al foil. The deposition of the metal (Al) onto the CNT sheet-Al foil was performed via sputtering (Figure S2 b). The Al-deposited CNT-Al foils were stacked repeatedly (19 times) and the normal Al foil covered the top of the stacked CNT-Al foils. They were sintered using spark plasma sintering (SPS). As the pristine Al foils (matrix) already have intrinsic anisotropic mechanical properties owing to the rolling direction, special care was required for fabrication and analysis. All the Al foils were tailored within a large Al foil, and their stacking orientations were the same. The tensile test specimens were tailored in the shape of a dog bone.

The average weight of a single layer of the as-drawn CNT sheet is 8 μg (measuring 50 layers of CNT sheets), which is equivalent to 0.15 vol% (19 CNT layers with 20 Al foil, 25 μm) in the final composite. The volume fraction (V_f) of the CNTs can be calculated using their density and added weight. We prepared highly dense CNT yarn from 30-layer CNT sheets by twisting (360° × 100 turns), as shown in Figure S2 c. The diameter of the CNT yarn is 188 μm and its density is 0.4 g/cm^3, which is similar to the value obtained in the previous studies i.e., 0.47 g/cm^3.[1] From these values, the calculated volume fraction is 0.0015 (0.15 vol%) in the final product. The concentration of CNTs can be controlled by changing the thickness of the metal foil. We used the commercial Al foils of thickness 25 μm, which is the minimum manageable, 38 μm, 100 μm.

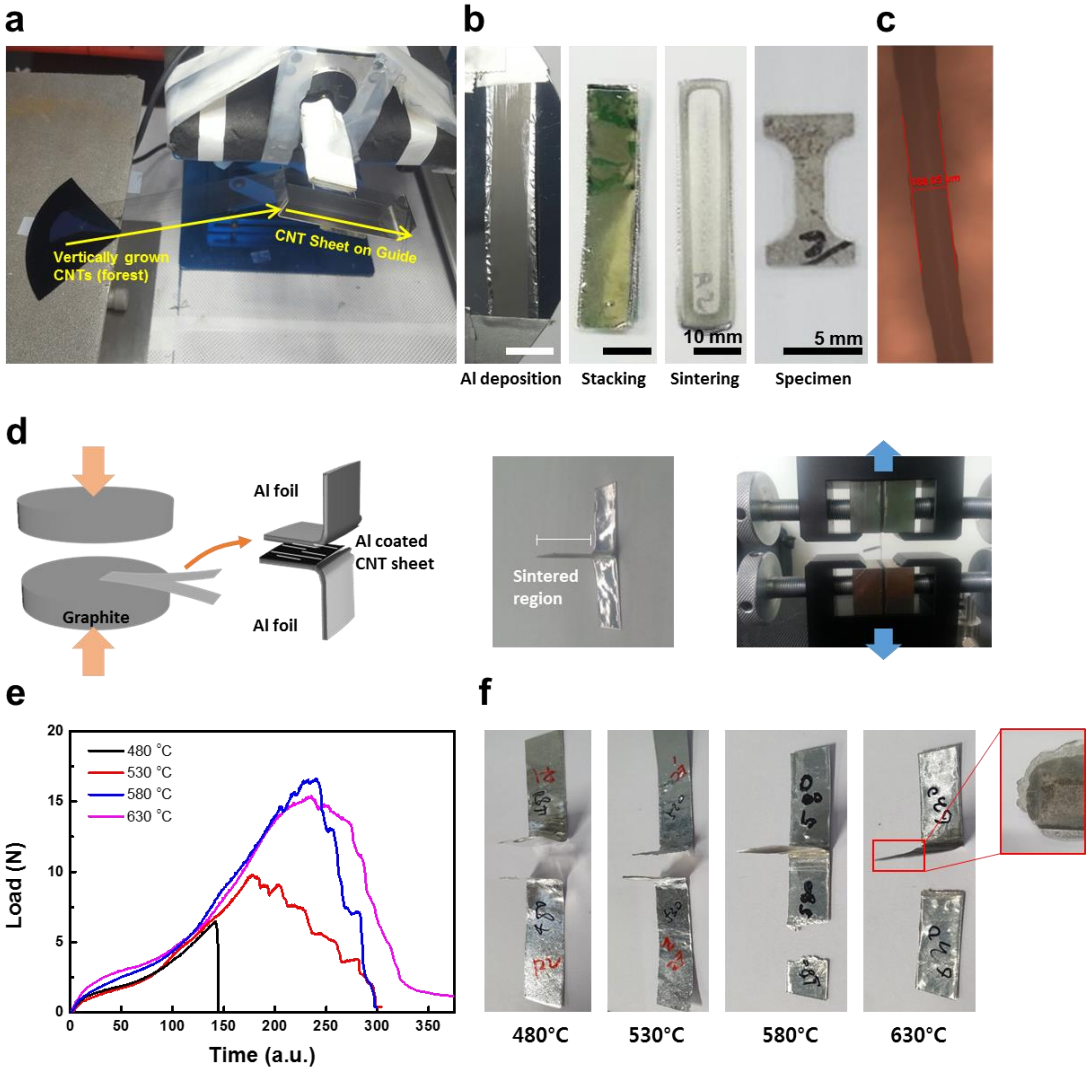

Figure S2. Photographs of fabrication process: (a) the mechanical pulling method for CNT sheet, (b) Al deposited CNT-Al foils, stacking method, Al-CNT composite sample after SPS, and tensile test specimen. The scale bar is 10 mm and 5 mm. (c) Optical image of the CNT yarn from 30-layer CNT sheets by twisting (360° × 100 turns). Peeling test for optimization of sintering temperature: (d) schematics of specimen preparation and peeling test, (e) test results of various sintering temperature conditions (480, 530, 580, 630 °C), and (f) photographs of the peeling specimens after the test.

The sintering temperature was optimized through a peeling test. Two Al foils were stacked with the Al-coated CNT sheet (stacking order: Al foil–CNT sheet-Al foil), and half of the foil was sintered (480 to 630 °C with 50 °C step), resulting in a T-shape specimen, as shown in

Figure S2 d. Using the universal test machine, we gripped both ends of the un-sintered region and applied a tensile load (peeling test). Figure S2 e shows the peeling test result. The maximum load increase in proportion to the sintering temperature. And the maximum loads of 580 and 630 ℃ conditions are nearly identical. Figure S2 f shows photographs of the peeling specimens after the test. Under 530 °C sintering condition, the peeling was generated on sintering part resulting that we obtained two L-shape specimens that were separated up and down. It indicates that there is no sintering behavior between two Al foils and CNT sheet. Further increase temperature (580, 630 °C), the cracking was generated in the non-sintered region. There is no peeling behavior in the sintered region, which is good evidence for successful sintering. However, in case of 630 °C condition, the partially molten part was observed in edge side of the specimen as shown in a red box image of Figure S2 f. Since the liquid phase of Al accelerate the reaction between Al and CNT, the Al-C compound can be formed excessively. From these result, we selected 580 °C as an optimum condition in our process.

➢ **Tensile test specimen**

As the tailored specimen for the tensile test is small as shown in Figure S2 b, the extension during the tensile test cannot be measured using the contact type extensometer. Therefore, firstly, we measured the machine extension, and modified it by the gauged extension measured using an optical microscope. Figure S3 a shows the photographs of the tensile specimen, and b shows the optical images for the selected area corresponding to the green dashed box in (a). In Figure S3 b, the upper image shows the specimen before the tensile test, where l_0 is an initial length between pre-marked lines. The lower image shows the specimen after the test, where l_t is a length between deformed-marked lines. The actual elongation was calculated using the gauged extension defined by $(l_t - l_0) / l_0$. Subsequently, the stress-strain curve was modified using the calculated elongation. Figure S3 c shows the stress-strain curves of raw Al. The black line represents the machine extension data, while the red line represents the modified actual elongation data.

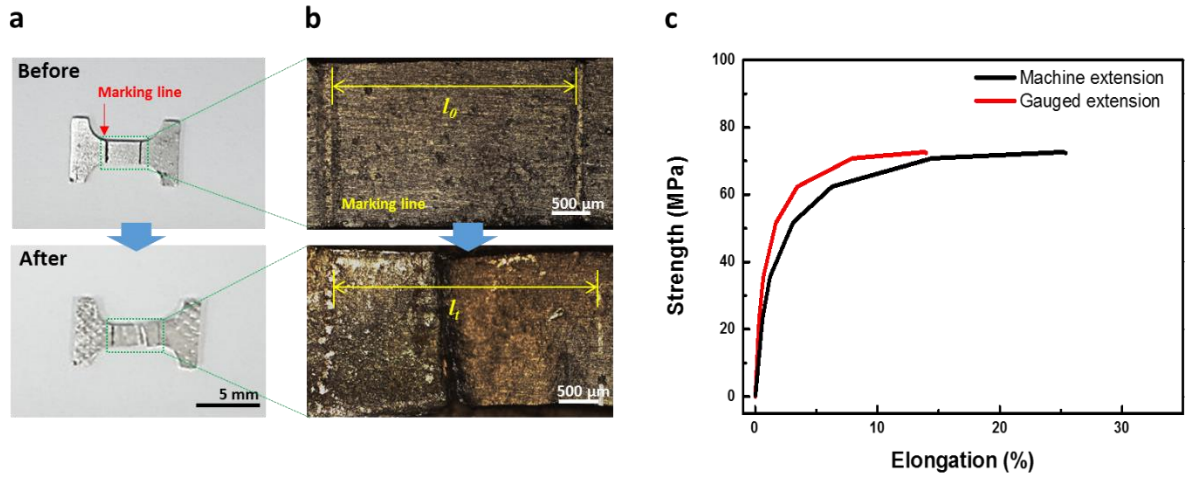

Figure S3. Tensile test specimen: (a) Photographs of the tensile specimen. (b) optical images of the tensile specimen for the selected area corresponding to the green dashed box in (a). Upper and lower images are for the specimen before and after the tensile test, respectively in (a-b). (c) Stress-strain curves of Al raw sample. The black and red lines represent the machine extension data and modified actual elongation data, respectively.

➢ **Morphology of pristine CNT and metal-deposited CNT sheet**

The average diameter of CVD-grown multi-wall CNTs is 15.3 nm with ± 1.3 standard deviation (Figure S4 a,b) and comprise of 16 graphitic walls (Figure S4 c,d) in average. As the thickness of the as-drawn CNT sheet is approximately 10 μm, as shown in Figure S5 a, a non-uniform deposition is observed between the top and bottom parts of the CNT sheet. To observe the bottom part, we peeled off the Al-deposited CNT sheet from the Al foil and thereafter turned it over by 180°. The diameter of the metal-deposited CNT is 70–180 nm in the top part (Figure S5 b) and 50–100 nm in the bottom part (Figure S5 c). Nevertheless, Al atoms are deposited on the entire CNT surface.

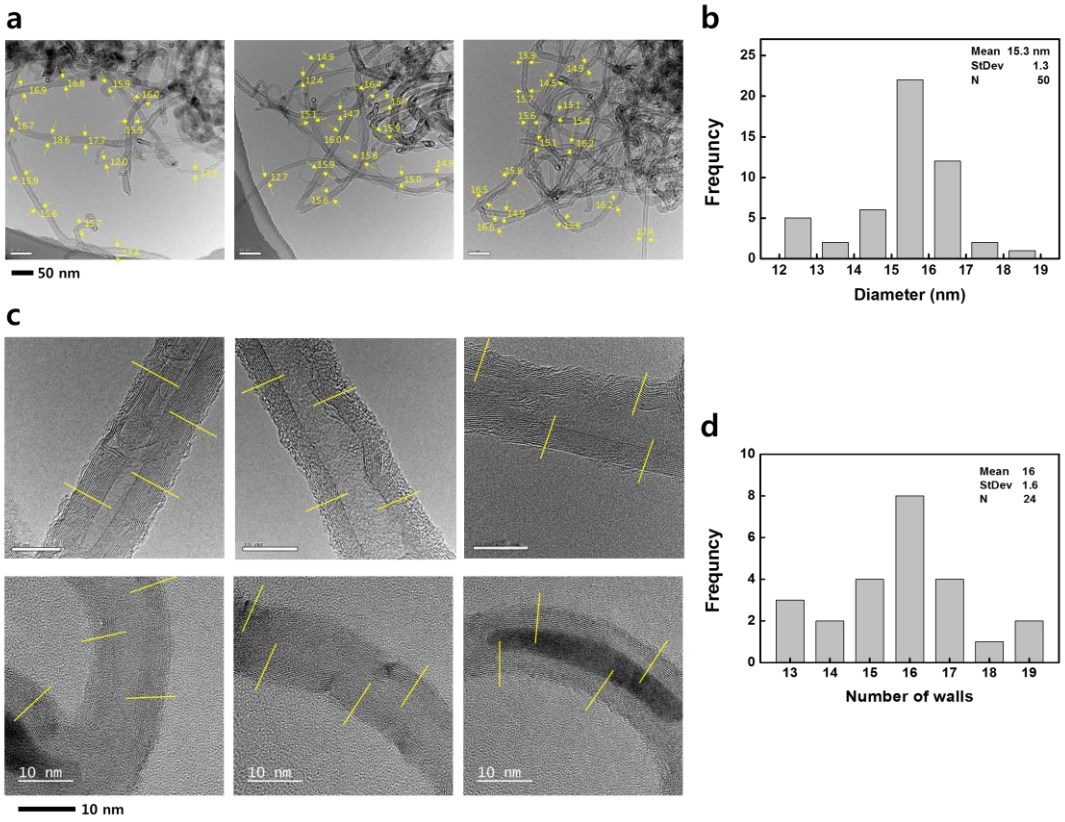

Figure S4. Information of pristine CNTs: (a) TEM images of pristine CNTs, (b) average diameter, (c) high-resolution TEM images of pristine CNTs, and (d) the average number of CNT walls.

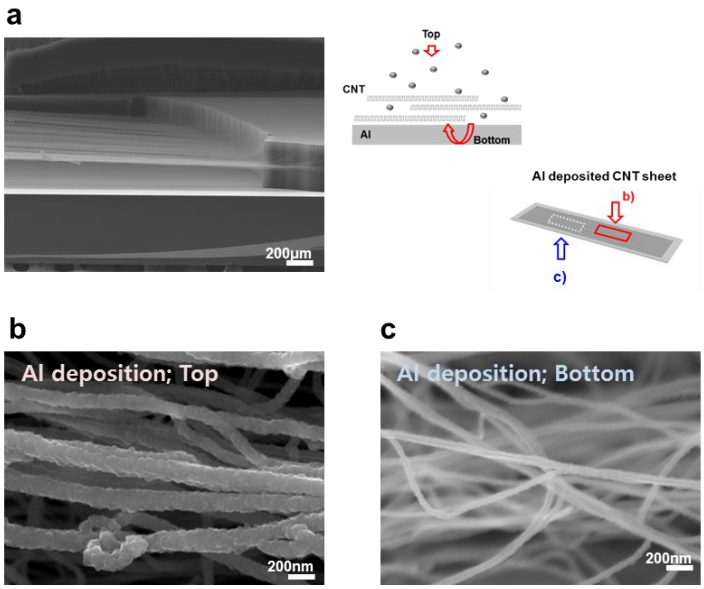

Figure S5. Scanning electron microscope image of (a) the side view of the as-drawn CNT sheet, (b) the top part of the Al-deposited CNT sheet, and (c) bottom part of the Al-deposited CNT sheet. Right side image of (a) is a schematic illustration of the metal deposition process.

➢ **Demonstration of CNT crystallinity and formation of Al-C compound at final process**

The Al-CNT composite was etched by acidic solution until all of the matrices is removed. And then it was filtered and dried. Figure S6 a is the SEM image of the filtered sample. The cylinder shape of CNTs was clearly observed. In addition, there are some residual products. The crystal information of residual products was verified by XRD measurement (Figure S6 b). The peaks corresponding to the Al_4C_3 and Al_2O_3 crystals were visible. We expected that the Al_4C_3 peaks are originating from the partially crystallized compounds on the interface, and the Al_2O_3 peaks are from the oxidation of aluminum during the etching process. Therefore, Al_4C_3 compounds are successfully formed. Figure S6 c shows the result of thermos-gravimetric analysis (TGA) of pristine and filtered CNT samples under the air. Although the burning temperature of CNTs in the filtered sample (near 560 °C) is a little bit lower than the pristine CNT's one (near 580 °C) because of some defects on CNT surface during process, the oxidation tendencies are same. This indicates that the initial CNT structures (crystallinity) are retained in the final process.

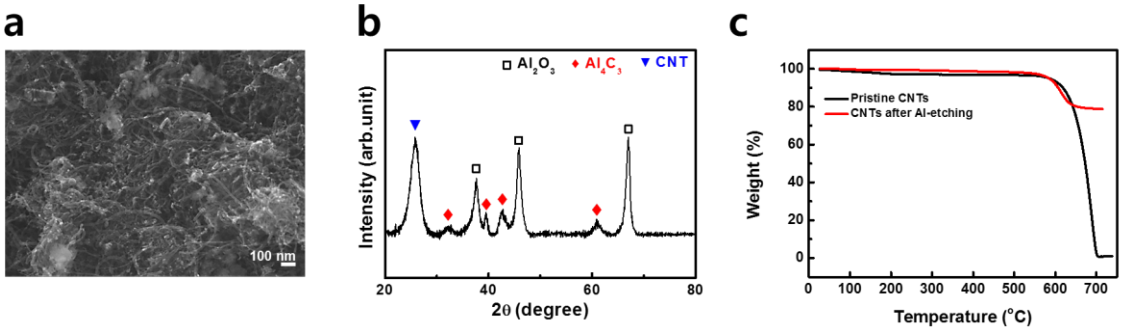

Figure S6. Remaining products after the etching process of Al-CNT composite: (a) SEM image of the filtered sample, (b) XRD result, (c) TGA result of the filtered sample compared with a pristine CNT.

Also, the formation of Al-C compounds in the Al-CNT composite is demonstrated using XPS measurement. Figure S7 shows the Al 2p peaks in the XPS spectra of raw Al (top) and Al-CNT composite (bottom). In both samples, we observe peaks at 73.1 eV and 75.6 eV, which are associated with the Al-O bond and Al metal bond, respectively. The Al-CNT composite sample shows a peak at 74.5 eV, which corresponds to the Al-C bond.[2]

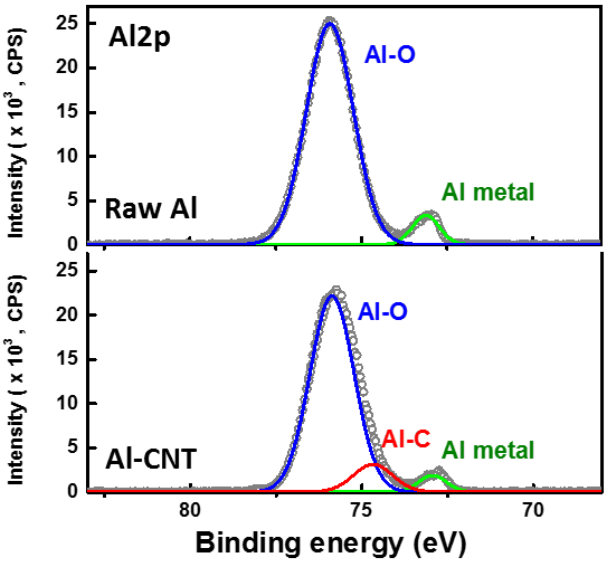

Figure S7. XPS patterns of (a) C 1s peak of the Al-CNT composite, (b) Al 2p peak of raw Al (top) and Al-CNT composite (bottom).

➢ **Microstructure of the Al-CNT composite**

Uniaxially aligned CNTs are observed using transmission electron microscopy (Figure S8 a, b). The yellow dashed arrow indicates the alignment direction. The high-magnification image (Figure S8 b) shows not only the aligned CNT bundles but also the interconnecting CNTs (green arrows). Such interconnecting CNTs connect the CNT bundles with each other, which is the main principle of continuous pulling of CNT sheets.[3]

Figure S9 a shows the individual CNTs after the final process. The CNTs are covered with Al-C compound layer which is distinguished by the yellow dashed line. Since the outermost carbon wall was consumed for a formation of the atomically fused and chemically bonded interface, the diameter of CNT should be changed (schematic in Figure S9 b). The average diameter of the retained CNT structure region is 14.5 nm (± 1.2 SD), as shown in Figure S9 c.

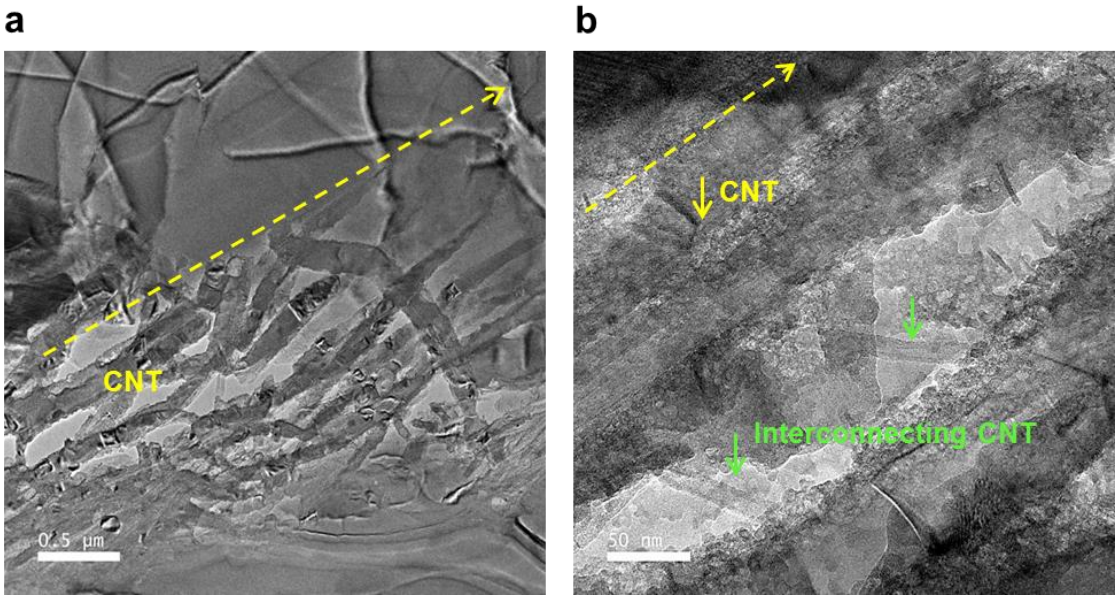

Figure S8. TEM image of the Al-CNT composite sample

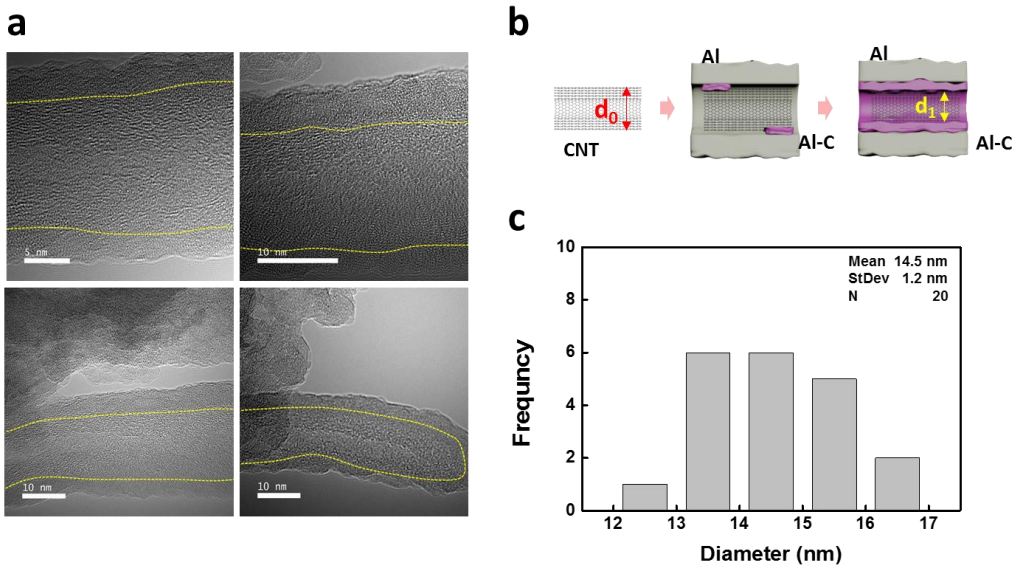

Figure S9. Diameter of CNTs in final processed sample: (a) TEM images of the individual CNT covered with Al-C compound layer, (b) schematic of degradation of CNTs during the formation of Al-C compound, and (c) result of retained CNT diameter in average.

➢ **Effect of metal deposition**

As the natural oxide present on the metal foil surface prevents the formation of the Al-C compound, the CNTs simply slip from the Al matrix during the tensile test owing to the weak bonds between the carbon atoms and the Al matrix, as shown in Figure S10 a. As a result, long CNTs were observed mainly in slip surface, as shown in Figure S11 a. However, the metal deposition process leads to a strong bond between the Al matrix and CNTs (formation of Al-C compound at the interface). During the sputtering process, the metal atoms are deposited on the CNT surface without any oxide due to the high vacuum condition. Subsequently, the deposited metal atoms react with CNTs during sintering. Consequently, the applied stress is effectively transferred to the CNTs during the tensile test (Figure S10 b), resulting in that the CNTs with short lengths and sharp ends are mainly present in the fracture surface owing to the failure of CNTs as shown in Figure S11 b.

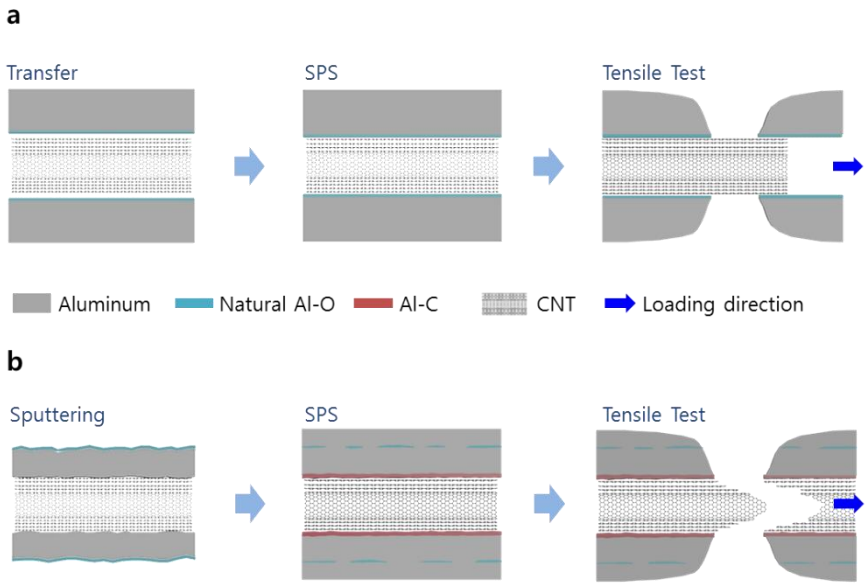

Figure S10. Schematic illustrations of the interaction between Al and CNT: (a) without the Al deposition process, (b) with Al deposition.

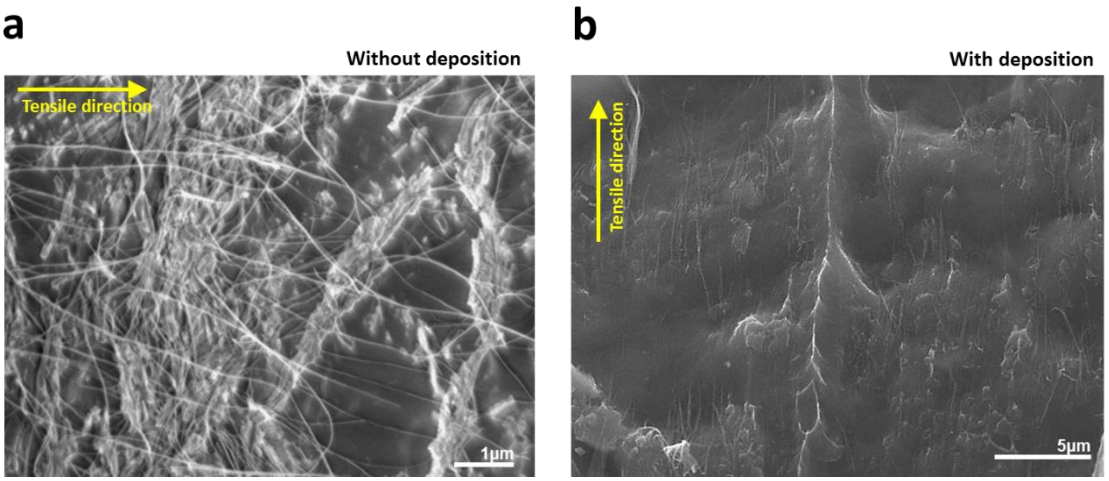

Figure S11. SEM image of the fracture surface of Al-0.15 vol% CNT composite sample (a) without and (b) with Al deposition process.

➢ Mechanical properties of Al-CNT composites

Table S1. Summary of the average mechanical properties of raw Al and Al-0.1 vol% CNT composites with angular dependence

Misorientation angle [θ]		Young's modulus		Yield strength		Tensile strength		Elongation	
		[GPa]	Improvement [%]	[MPa]	Improvement [%]	[MPa]	Improvement [%]	[%]	Improvement [%]
0 °	RAW	66.5		38.2		63.7		18.2	
	Al-CNT	67.8	1.95↑	40.1	4.97↑	69.9	9.75↑	17.6	-3.30↓
45 °	RAW	63.3		39.0		62.6		16.2	
	Al-CNT	63.9	0.95↑	40.1	2.82↑	67.3	7.44↑	16.0	-1.23↓
90 °	RAW	66.1		33.6		62.2		15.6	
	Al-CNT	66.0	-0.15↓	34.5	2.68↑	64.1	3.05↑	15.4	-1.28↓

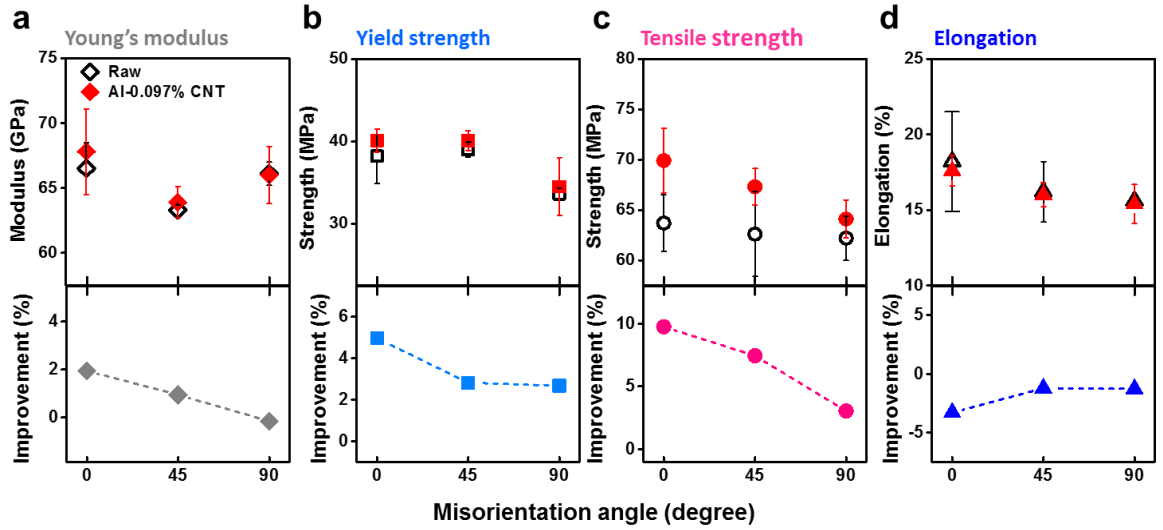

Figure S12. Angular dependence of mechanical properties of raw Al and the Al-0.1 vol% CNT composite: (a) Young's modulus, (b) yield strength, (c) tensile strength, and (d) elongation. The upper panels represent the absolute values of mechanical properties. The raw Al and Al-CNT composite are marked with black open symbols and red solid symbols, respectively. The lower panels represent the relative improvement.

Table S2. Summary of the average mechanical properties of raw Al and Al-0.03 vol% CNT composites with angular dependence

Misorientation angle [θ]		Young's modulus		Yield strength		Tensile strength		Elongation	
		[GPa]	Improvement [%]	[MPa]	Improvement [%]	[MPa]	Improvement [%]	[%]	Improvement [%]
0°	RAW	63.7		25.8		53.4		31.1	
	Al-CNT	64.2	0.78↑	25.9	0.39↑	54.1	1.44↑	30.7	-1.29↓
45°	RAW	65.0		26.0		54.0		30.8	
	Al-CNT	65.2	0.31↑	26.3	1.15↑	55.2	2.22↑	30.6	-0.65↓
90°	RAW	67.0		26.0		52.4		28.2	
	Al-CNT	67.4	0.60↑	26.1	0.38↑	52.3	-0.19↓	28.3	0.35↑

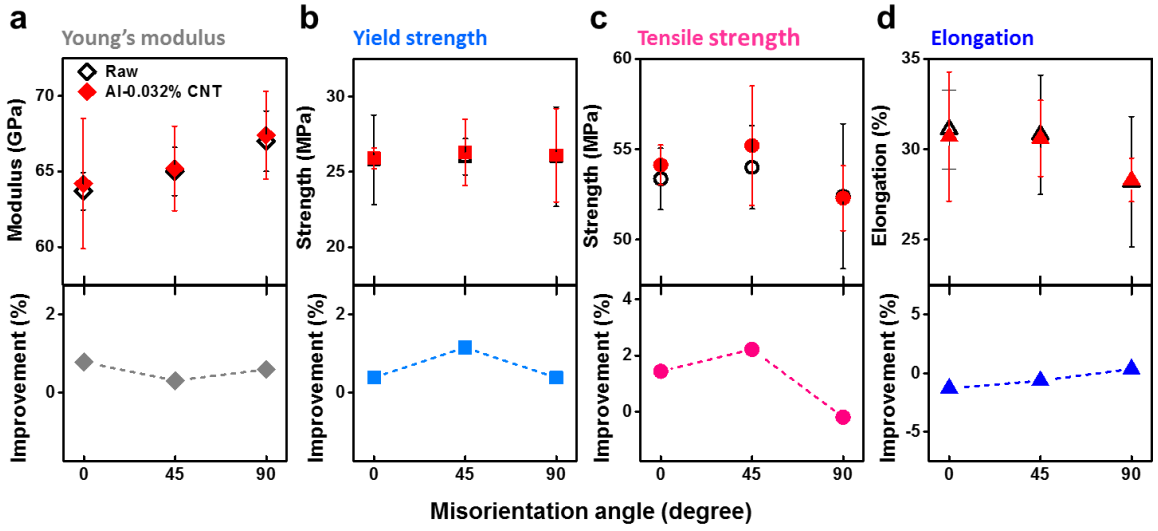

Figure S13. Angular dependence of mechanical properties of raw Al and the Al-0.03 vol% CNT composite: (a) Young's modulus, (b) yield strength, (c) tensile strength, and (d) elongation. The upper panels represent the absolute values of mechanical properties. The raw Al and Al-CNT composite are marked with black open symbols and red solid symbols, respectively. The lower panels represent the relative improvement.

➢ **Work hardening exponent**

Figure S14 shows the difference of work hardening exponents ($\Delta n = n_{composite} - n_{raw}$) / n_{raw} × 100%). Δn is −0.9% at 0°, 0.6% at 45°, and −2.2% at 90°. The change in n is not noticeable, regardless of misorientation. Thus, the strengthening effect owing to the two dislocation-related mechanisms (Orowan looping and thermal mismatch mechanism) is negligible.

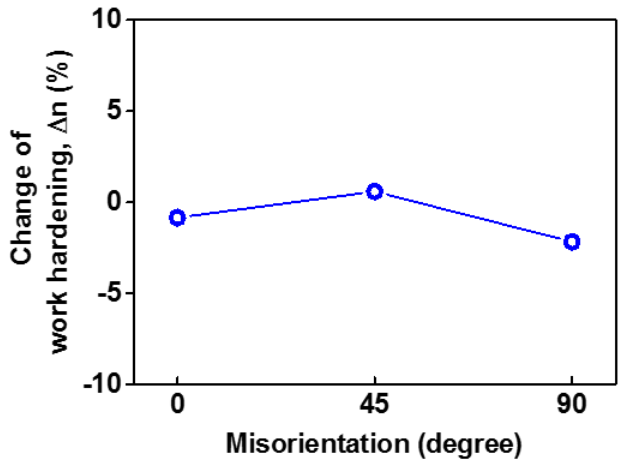

Figure S14. Change in the work hardening exponent (Δn) with angular dependence.

- **Grain size**

Figure S15 a and b are the XRD results of raw Al and Al-0.15vol%CNT composite, respectively, which were used in the Halder–Wagner equation for the estimation of average grain size. The calculated crystal sizes of raw Al and the composite are 476 nm and 484 nm, respectively. Figure S15 c and d are the electron back scatter diffraction (EBSD) results of two samples. The cross-sectional samples were polished with SiC papers (800, 1200 grit) and a polycrystalline diamond (3, 1 μm) suspension. In the raw Al sample, the average grain size is 782 nm. Despite the adding CNT, the average grain size of Al-CNT composite is similar (764 nm) with the raw sample. Owing to the low crystallinity of the stacking part, the black line and empty section were observed in the image quality map and grain map, respectively, of both samples. The black line corresponds to the stacking part between two Al foils in the raw sample. On the other hand, the black line corresponds to the localized CNT part in the Al-CNT composite sample. Owing to the thickness of CNT sheet (under 1 μm, grain map in Figure S15 d), the stacking part of Al-CNT composite is more clearly observed. The thickness of the as-drawn CNT sheet is approximately 10 μm. The thickness of the localized CNT region is submicron. In addition, there is no positional gradient of grain sizes between the central position of the foil and the immediate side of localized CNT. Such XRD and EBSD results indicate that the grain refinement does not occur owing to the artificial localization structure and deformation-free process.

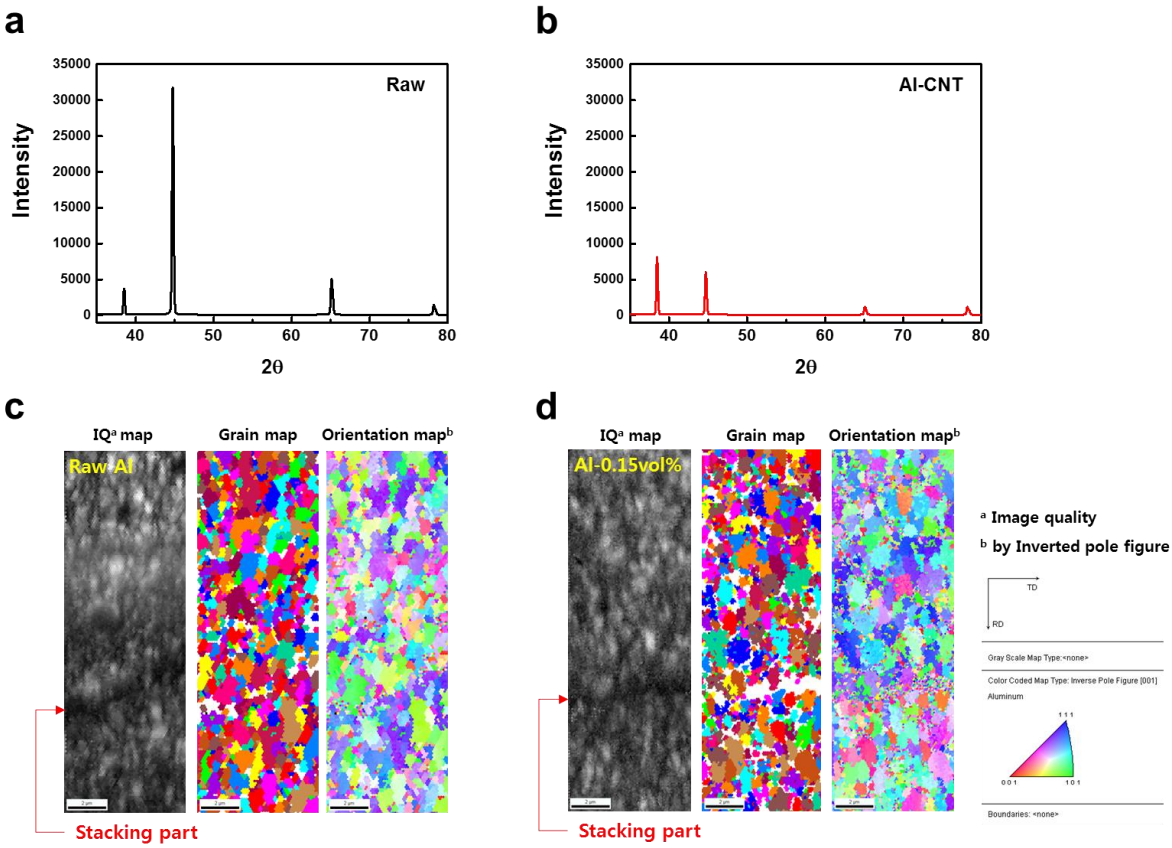

Figure S15. Micro-structure analysis: XRD result of (a) raw Al and (b) Al-0.15 vol% CNT. EBSD result of (c) raw Al and (d) Al-0.15 vol% CNT.

- **Failure criterion with various dispersion arrays**

In the uniaxially aligned fiber composite, the fracture is initiated and propagated along with the weakest fracture mode among various fracture modes including reinforcement fracture, matrix fracture, and shear fracture of the matrix, referred to the failure criterion. At the iso-strain state (misorientation angle = 0°), since the same tensile load is applied to the entire area, it should be included the fracture of reinforcement, resulting in that the propagation direction is perpendicular with loading direction. At the 45° of misorientation angle, fracture propagates along the direction of shear fracture of the matrix without reinforcement fracture because the reinforcement is much stronger than the matrix. At iso-stress state (misorientation angle = 90°), the fracture is generated in the matrix without reinforcement fracture owing to the same reason of the 45° of misorientation angle. These phenomena are summarized in Figure S16. In addition, the uniform-, random-, and localized array of fiber dispersion are illustrated in Figure S16. It is assumed here that tensile load is applied uniformly on an entire cross-section of specimen. In other words, there is no load gradient. At that time, even if the degree of dispersion varies, the direction of fracture propagation is the same because the weakest plane does not change.

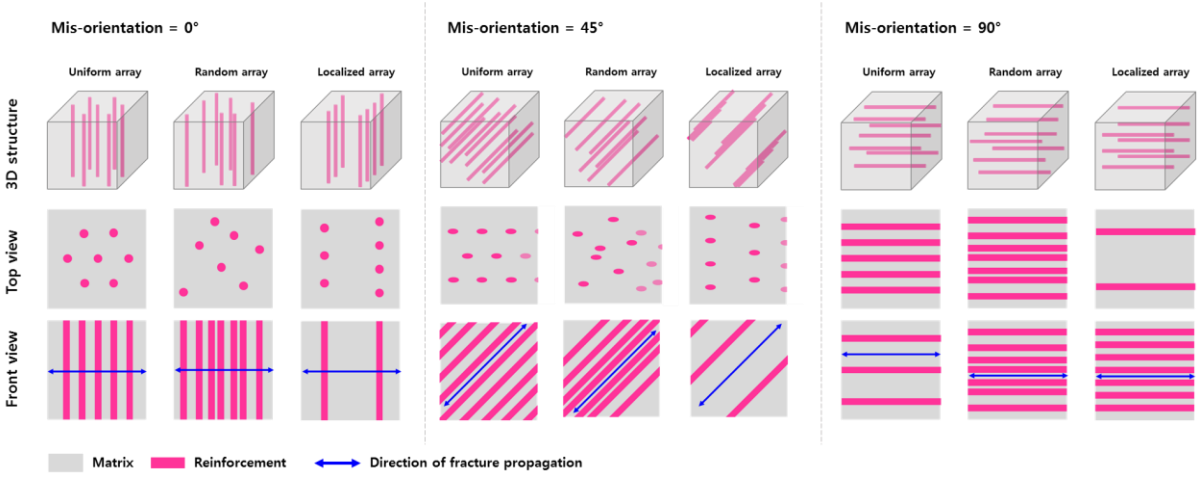

Figure S16. Failure criterion of uniaxially aligned composite with various dispersion array models including uniform-, random-, and localized array.

- **Fracture surface at the iso-stress state sample**

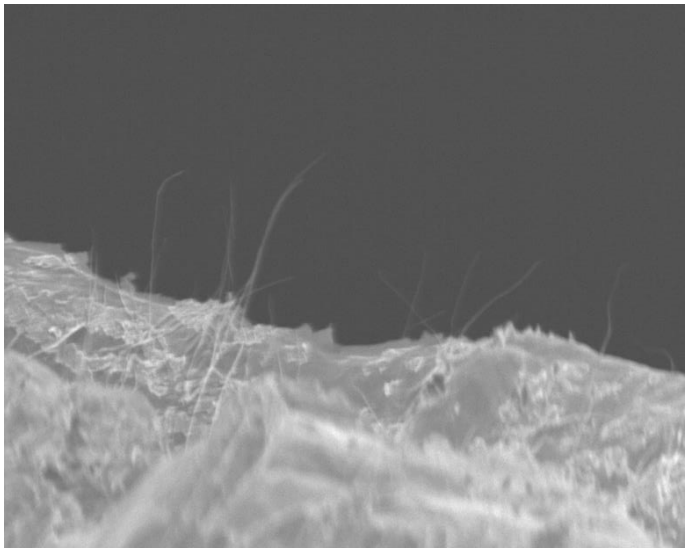

Figure S17. SEM image of the fracture surface of Al-0.15vol% CNT composite sample at iso-stress state

➢ Failure propagation of CNT under tensile load

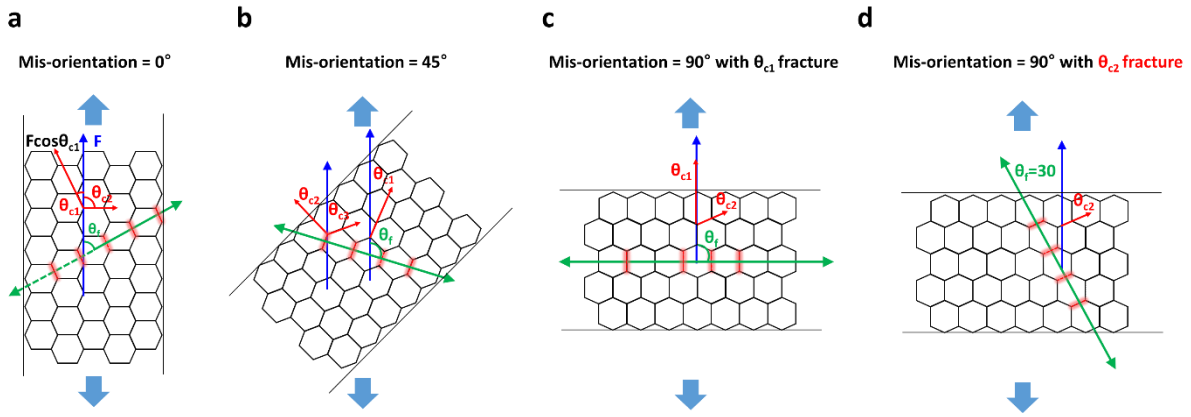

Figure S18. Schematic of the armchair CNT under tensile load; (a) misorientation angle = 0°, (b) misorientation angle = 45°, (c) misorientation angle = 90°. Arrows represent the applied loading direction (red), fracture propagation direction (green), and tensile load direction (blue). The possible C-C de-bond lattice is represented by the red dashed line with highlighting. $\theta_{c1\text{-}3}$ are the applied loading angles, and θ_f is the fracture propagation angle. These represent the tilt angles from the tensile load direction. Comparison between two different fracture angles: fracture propagation along (c) θ_{c1} lattice direction and (d) θ_{c2} lattice direction.

Table S3. Angular dependence of the failure parameters of the armchair CNT under tensile load

Item	Symbol	Values								
Misorientation angle of CNT bridge	θ_B	0	15	30	45	60	75 [c]		90 [c]	
Applied loading angle into C-C bonds	θ_{c1}	30	15	0	15	30	**15**	15	**0**	0
	θ_{c2}	30	45	60	45	30	45	**45**	60	**60**
	θ_{c3}	90	75	60	75	90	75	75	60	60
Fracture propagation angle	θ_f	60	75	90	75	60	45	45	90	30
Circumference along the CNT failure	P(nm)	49.2	49.2	49.2	49.2	49.2	5.2E+17	49.2	5.2E+17	49.2
Number of C-C bonds on failure circumference [a]	$n_{c\text{-}c}$	197.6	197.6	197.6	197.6	197.6	2.1E+18	197.6	2.1E+18	197.6
Normalized require force for C-C de-bond	$1/(\cos\theta_{c1})$	1.2	1.0	1.0	1.0	1.2	1.0	1.4	1.0	2.0
Total require force for CNT failure [b]	F_T	228.2	204.6	197.6	204.6	228.2	2.2E+18	278.0.	2.1E+18	395.2

a) Number of C-C bonds on failure circumference ($n_{c\text{-}c}$) = Circumference (P) / Distance between C-C bonds ($d_{c\text{-}c}$ = 0.249 nm)
b) Total required force for CNT failure (F_T) = $n_{c\text{-}c} \times 1/(\cos\theta_{c1})$
c) Two different fracture angles under the same θ_B. The main loading angles are boldfaced.

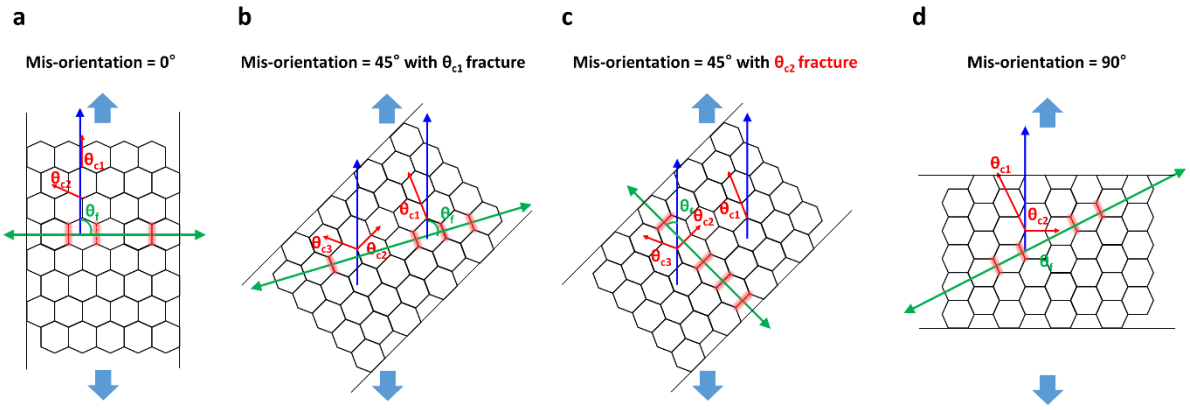

Figure S19. Schematic of the zigzag CNT under tensile load; (a) misorentation angle = 0°, (b) misorentation angle = 45°, (d) misorentation angle = 90°. Comparison between two different fracture angles: fracture propagation along (b) θ_{c1} lattice direction and (c) θ_{c2} lattice direction.

Table S4. Angular dependence of failure parameters of the zigzag CNT under tensile load

Item	Symbol	Values							
Misorientation angle of CNT bridge	θ_B	0	15	30	45 [c]		60	75	90
Applied loading angle into C-C bonds	θ_{c1}	0	15	30	**15**	15	0	15	30
	θ_{c2}	60	45	30	45	**45**	60	45	30
	θ_{c3}	60	75	90	75	75	60	75	90
Fracture propagation angle	θ_f	90	75	60	75	45	90	75	60
Circumference along the CNT failure	P(nm)	45.6	45.6	45.6	72.0	45.6	45.6	45.6	72.0
Number of C-C bonds on failure circumference [a]	$n_{c\text{-}c}$	182.9	182.9	182.9	289.3	182.9	182.9	182.9	289.3
Normalized require force for C-C de-bond	$1/(\cos\theta_{c1})$	1.0	1.0	1.2	1.0	1.4	1.0	1.0	1.2
Total require force for CNT failure [b]	F_T	182.9	189.4	211.2	299.5	258.7	182.9	189.4	334.0

a) Number of C-C bonds on failure circumference ($n_{c\text{-}c}$) = Circumference (P) / Distance between C-C bonds ($d_{c\text{-}c}$ = 0.249 nm)
b) Total required force for CNT failure (F_T) = $n_{c\text{-}c} \times 1/(\cos\theta_{c1})$
c) Two different fracture angles under the same θ_B. The main loading angles are boldfaced.

- **Calculation of volume fraction of CNT bridge**

The average tensile strength ($\sigma_{aver.}$) of a randomly oriented 1D composite can be predicted by $\sigma_{aver.} = (\sigma_{max} \cdot \sigma_{min})^{1/2}$. The minimum tensile strength of the CNT bridge-reinforced part is calculated by $\sigma_{min} = \sigma_{CNT} V_{CB} + (\sigma_M)_{\epsilon^*CNT} (1-V_{CB})$, and the maximum is calculated by $\sigma_{max} = \alpha\sigma_{CNT}V_{CB} + (\sigma_M)_{\epsilon^*CNT} (1-V_{CB})$.

Thus,

$\sigma_{aver.}^2 = [\sigma_{CNT} V_{CB} + (\sigma_M)_{\epsilon^*CNT} (1-V_{CB})]^* [\alpha\sigma_{CNT}V_{CB} + (\sigma_M)_{\epsilon^*CNT} (1-V_{CB})]$

$= V_{CB}^2[\alpha\sigma_{CNT}^2 - \sigma_{CNT}(\sigma_M)_{\epsilon^*CNT} (1+\alpha) + (\sigma_M)_{\epsilon^*CNT}^2] + V_{CB}[\sigma_{CNT}(\sigma_M)_{\epsilon^*CNT} (1+\alpha) + 2(\sigma_M)_{\epsilon^*CNT}^2] + (\sigma_M)_{\epsilon^*CNT}^2$

If,

$A= \alpha\sigma_{CNT}^2 - \sigma_{CNT}(\sigma_M)_{\epsilon^*CNT} (1+\alpha) + (\sigma_M)_{\epsilon^*CNT}^2$

$B= \sigma_{CNT}(\sigma_M)_{\epsilon^*CNT} (1+\alpha) + 2(\sigma_M)_{\epsilon^*CNT}^2$

$C= (\sigma_M)_{\epsilon^*CNT}^2$

$\sigma_{aver.}^2 = V_{CB}^2A + V_{CB}B + C$

In the Al-0.15vol% CNT (25 μm) composite, $\sigma_{aver.}$ at the iso-stress condition is 70.4 MPa and $(\sigma_M)_{\epsilon^*CNT}$ is 61.9 MPa (maximum stress at the fracture strain of CNTs, ϵ^*_{CNT} = 9.9%). The calculated V_{CB} is 0.00045. In the Al-0.1vol% CNT (38 μm), $\sigma_{aver.}$ at the iso-stress condition is 64.1 MPa and $(\sigma_M)_{\epsilon^*CNT}$ is 59.1 MPa. The calculated V_{CB} is 0.00032.

- **Modified failure criterion**

The failure criterion is expressed as follows (Equation 11 in the main manuscript),

$$\sigma_x = \left[\frac{cos^4\theta}{\sigma_{\parallel}{}^2} + cos^2\theta sin^2\theta \left(\frac{1}{\tau_M{}^2} - \frac{1}{\sigma_{\parallel}{}^2}\right) + \frac{sin^4\theta}{\sigma_{\perp}{}^2}\right]^{-\frac{1}{2}} \quad (11)$$

where the tensile strength ($\sigma_{\parallel}$) of the iso-strain condition can be calculated using Equation 12 in the main manuscript,

$$\sigma_{\parallel} = \sigma_{CNT}V_{CNT} + (\sigma_M)_{\epsilon^*_{CNT}}V_M \quad (12)$$

Here, $(\sigma_M)_{\epsilon^*_{CNT}}$ is the maximum stress at the fracture strain of CNTs, σ_M is the average experimental result for all raw samples.

In the Al-0.15vol% CNT composite (25 μm), σ_M is 67.6 MPa and $(\sigma_M)_{\epsilon^*_{CNT}}$ is 65.9 MPa. The calculated $\sigma_{\parallel}$ is 82.3 MPa (improved by 21.8%). In the Al-0.1vol CNT (38 μm), σ_M is 62.8 MPa and the calculated $(\sigma_M)_{\epsilon^*_{CNT}}$ is 59.0 MPa. The calculated $\sigma_{\parallel}$ is 70.0 MPa (improved by 11.4%).

In the traditional failure criterion, the shear fracture (τ_M) can be replaced by $\sigma_{//}$ which is calculated using Equation S1,

$$\sigma_{//} = \tau_M(1 - V_{CB}) + \sigma_{CNT}V_{CB} \quad (S1)$$

The value of $\sigma_{//}$ is also modulated by changing the misorientation angle of the CNT bridge (θ_B). Thus, $\sigma_{//aver.} = (\sigma_{//max}\cdot\sigma_{//min})^{1/2}$, where $\sigma_{//min} = \tau_M(1\text{-}V_{CB}) + \sigma_{CNT}V_{CB}$, $\sigma_{//max} = \tau_M(1\text{-}V_{CB}) + \alpha\sigma_{CNT}V_{CB}$. τ_M is defined by $0.6 \times \sigma_M$, and α is 2.16. As a result, $\sigma_{//aver.}$ is 48.0 MPa in the Al-0.15vol% CNT composite (40.4 MPa in Al-0.1vol% CNT composite).

In the failure criterion, the tensile strength at iso-stress ($\sigma_{\perp}$) is modified by $\sigma_M\cdot\Delta M$, where ΔM is the improvement in the tensile strength from the experimental result. $\sigma_{\perp}$ is 74.9 MPa (ΔM = 0.11) and 64.8 MPa (ΔM = 0.03) for the Al-0.15% CNT and Al-0.1% CNT composite, respectively.

➢ **Anisotropic mechanical properties of Al-0.1 vol% CNT composite**

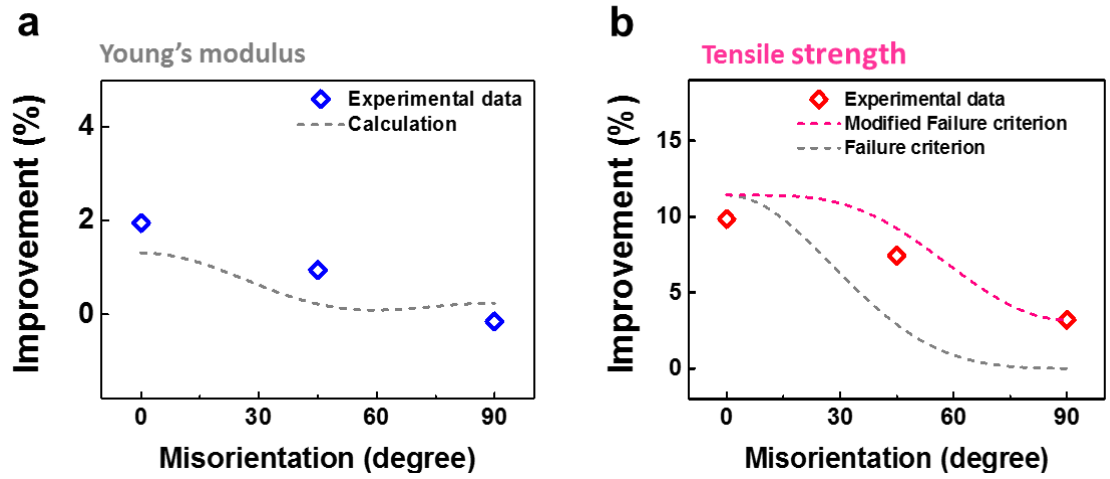

Figure S20. Comparison of improvement of mechanical properties of Al-0.1 vol% CNT composite between the calculation (dashed line) and experimental (open rhombus symbols) values : (a) Young's modulus, the calculation (gray dashed line) is plotted by Equation 8 in the main manuscript. (b) tensile strength, the gray and magenta dashed lines are calculated by the failure criterion (Equation 11 in the main manuscript) and the modified failure criterion, respectively.

➢ **Defect generation in the interface**

During the tensile test, the difference between the Poisson's ratios of Al (0.33), Al-C compound (Al_4C_3, 0.18),[4] and CNT (in-plane, 0.19)[5] leads to the generation of defect sites, as shown in Figure S21. The generated defects reduce the elongation of the composite. As the interface area is constant regardless of the misorientation angle, the elongation has near-isotopic behavior.

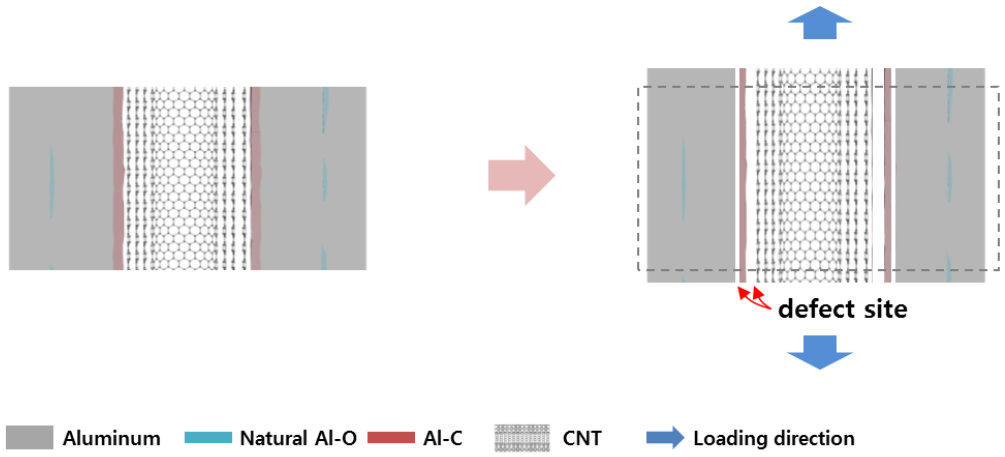

Figure S21. Schematic illustration of the defect generation in interfaces during the tensile test

➢ Strengthening efficiency (R) and elongation of Al-CNT composites

Table S5. Summary of the strengthening efficiency and elongation in our study and previous studies. It includes the aspect ratio of CNT and fabrication process.

Reference No. [a]	CNT concentration [wt%]	Tensile strength [MPa] [b]		Strengthening Efficiency (R)	Elongation [%]		Change in elongation [%]	Dimension of pristine CNT			Fabrication Process [c]
		σ_{raw}	$\sigma_{composite}$		ε_{raw}	$\varepsilon_{composite}$		Length [nm]	Diameter [nm]	Aspect ratio	
Our	0.02	71	85	1,005	13.1	12.3	−5.9	330,000	15	22,000	Superalignment Method
	0.014	64	70	696	18.2	17.6	-3.3				
3	4.5	123	420	53.7	24.0	5.3	−77.9	-	-	-	In-situ growth, BM, EX
7	2.0	285	345	10.6	8.6	5.7	−33.7	3,500	140	25	BM, EX
8	0.5	130	142	18.5	25.0	18.0	−28.0	3,500	140	25	BM, Hot rolling
10	1.0	448	560	25.0	14.4	10.2	−29.2	10,000	50	200	BM(with LN), HIP, EX
14	0.5	153	174	27.5	35.0	34.0	−2.9	10,000	80	125	Blending , SPS, EX
16	0.2	92	114	119.6	21.0	9.0	−57.1	5,000	20	250	Wet mixing, HP, Melt B, EX
50	1.0	229	265	15.7	2.8	1.7	−39.3	20,000	10	2,000	SiC coating, BM, Melt B, DC
51	1.0	384	474	23.4	16.5	3.0	−81.8	50,000	30	1,667	Stirring & Ultrasonic, BM, CP
52	2.0	160	251	28.4	19.6	15.6	−20.4	10,000	70	143	Spray pyrolysis method, BM, EX
53	6.5	140	322	20.0	8.9	0.7	−92.1	20,000	15	1,333	In-situ growth, Sinter
54	2.0	98	184	43.9	2.5	2.8	12.0	10,000	10	1,000	Blending, CP, ECAP
55	1.0	388	522	34.5	19.5	18.5	−5.1	500	30	17	BM ,CIP, EX
56	1.5	311	408	20.8	10.2	4.0	−60.8	2,500	22.5	111	BM, CP, EX
57	2.0	169	333	48.8	10.2	5.2	−49.0	7,000	140	50	BM, EX
58	0.5	185	217	34.6	5.0	3.0	−40.0	5,000	15	333	BM, HP, Forging
59	3.0	118	428	87.6	25.0	3.7	−85.2	-	-	-	BM, HP, EX

[a] Reference No. in main paper

[b] Tensile strength and elongation values have been obtained from the maximum experimental results

[c] BM: Ball Milling, EX: Extrusion, LN: Liquid Nitrogen, HIP: Hot Isostatic Pressing, SPS: Spark Plasma Sintering, HP: Hot Press, Melt B: Melt Blending, DC: Die-Casting, CP: Cold Press, ECAP: Equal Channel Angular Pressing, CIP: Cold Isostatic Pressing

➢ **Thickness dependence of volume fraction of CNT**

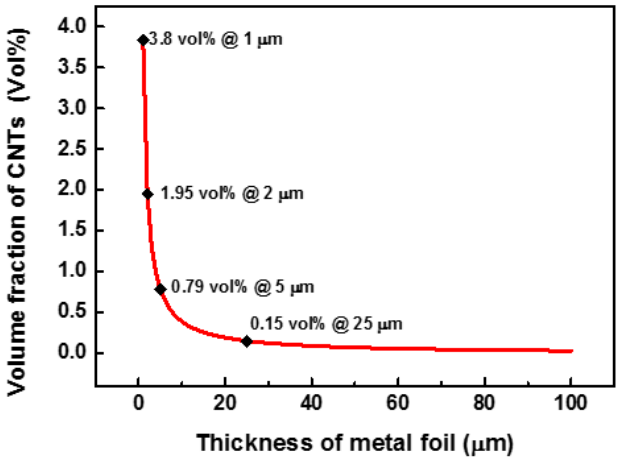

Figure S22. Thickness dependence of the volume fraction of CNT

References

[1] Q. Liu, M. Li, Y. Gu, Y. Zhang, S. Wang, Q. Li, et al., Highly aligned dense carbon nanotube sheets induced by multiple stretching and pressing, Nanoscale 2014;6(8):4338-44.

[2] C. Hinnen, D. Imbert, J.M. Siffre, P. Marcus, An in situ XPS study of sputter-deposited aluminium thin films on graphite, Applied Surface Science 1994;78:219-231.

[3] A.A. Kuznetsov, A.F. Fonseca, R.H. Baughman, A.A. Zakhidov, Structural model for dry-drawing of sheets and yarns from carbon nanotube forests, ACS Nano 2011;5(2):985-93.

[4] L. Sun, Y. Gao, K. Yoshida, T. Yano, W. Wang, Prediction on structural, mechanical and thermal properties of Al4SiC4, Al4C3 and 4H-SiC under high pressure by first-principles calculation, Modern Physics Letters B 2017;31(09):1750080.

[5] A. Pantano, M.C. Boyce, D.M. Parks, Mechanics of Axial Compression of Single and Multi-Wall Carbon Nanotubes, Journal of Engineering Materials and Technology 2004;126(3):279.